

Erythro–myeloid progenitors contribute endothelial cells to blood vessels

Alice Plein^{1,3}, Alessandro Fantin^{1,3}, Laura Denti¹, Jeffrey W. Pollard² & Christiana Ruhrberg^{1*}

The earliest blood vessels in mammalian embryos are formed when endothelial cells differentiate from angioblasts and coalesce into tubular networks. Thereafter, the endothelium is thought to expand solely by proliferation of pre-existing endothelial cells. Here we show that a complementary source of endothelial cells is recruited into pre-existing vasculature after differentiation from the earliest precursors of erythrocytes, megakaryocytes and macrophages, the erythro–myeloid progenitors (EMPs) that are born in the yolk sac. A first wave of EMPs contributes endothelial cells to the yolk sac endothelium, and a second wave of EMPs colonizes the embryo and contributes endothelial cells to intraembryonic endothelium in multiple organs, where they persist into adulthood. By demonstrating that EMPs constitute a hitherto unrecognized source of endothelial cells, we reveal that embryonic blood vascular endothelium expands in a dual mechanism that involves both the proliferation of pre-existing endothelial cells and the incorporation of endothelial cells derived from haematopoietic precursors.

Blood vessels distribute oxygen, nutrients, hormones and immune cells through the vertebrate body and help to remove waste molecules. Accordingly, the formation of functional blood vessels during embryogenesis is a prerequisite for vertebrate life. Endothelial cells (ECs) form the inner lining of blood vessels; they first arise from mesenchymal precursors termed angioblasts on embryonic day (E)7.0 in mice¹. After condensing into the yolk sac vasculature and paired dorsal aortae, ECs proliferate within existing endothelium to increase vascular diameter, sprout into avascular tissue areas or remodel into smaller vessels by intussusceptive growth¹. The current consensus is therefore that embryonic ECs are a self-contained cell lineage that expands without contribution from new angioblasts or circulating precursors. By contrast, circulating endothelial progenitors have been proposed to exist in adult vertebrates, although their relationship to myeloid cells remains controversial².

In addition to their primary roles in the innate immune system, myeloid cells such as monocytes and macrophages also modulate vascular growth³. For example, the tissue-resident macrophages of the embryonic mouse brain, termed microglia, contact ECs at the tips of neighbouring vessel sprouts to promote their anastomosis into perfused vessel loops⁴. By contrast, no direct contribution of myeloid cells to embryonic vascular endothelium has been reported; thus, genetic lineage tracing with myeloid *Vav* or *Lyz2* (also known as *Lysm*) promoters does not mark embryonic blood vascular endothelium in mice^{5,6}.

Most tissue-resident macrophages arise from EMPs that form in the extra-embryonic yolk sac during embryogenesis and also serve as precursors for erythrocytes and megakaryocytes^{7–11}. In mice, an early wave of EMPs, also referred to as primitive haematopoietic progenitors, buds from the yolk sac endothelium between E7.0 and E8.25 and differentiates by E9.0 without monocytic intermediates into yolk sac macrophages^{7,10,12–14}. These macrophages colonize the embryo proper to generate tissue-resident macrophages, such as microglia in the brain or Langerhans cells in the epidermis¹³. A later wave of EMPs buds from the yolk sac endothelium from E8.25 onwards and colonizes the liver after the embryonic circulation has been established^{7,8,11,14,15}. These later-born EMPs expand in the liver into monocytes that

subsequently differentiate into tissue-resident macrophages in many organs except the brain^{7,13}.

Csflr lineage tracing identifies an EC subset

To target early EMPs^{7,10,12}, microglia^{16,17} and other differentiated myeloid cells¹⁸, we and others have used a transgene that expresses CRE recombinase under the promoter for the myeloid lineage gene *Csflr* (also known as *Fms*), which encodes the colony-stimulating factor 1 receptor CSF1R. Microglia appear as single YFP⁺ cells in hindbrains from *Csflr-iCre* mouse embryos carrying the *Rosa^{YFP}* recombination reporter, with microglia and ECs also stained for isolectin B4 (IB4)¹⁶ (Fig. 1a). As previously shown⁴, the number of IB4⁺YFP⁺ microglia peaked in the hindbrain subventricular zone at E11.5, when vessels fuse into the subventricular vascular plexus (SVP) (Fig. 1b). Unexpectedly, we also observed sporadic, elongated IB4⁺YFP⁺ cells that appeared bound into the endothelium and increased steadily in number during SVP expansion (Fig. 1a–c; Extended Data Fig. 1a). *Csflr-iCre* targeting of vessel-bound cells was not an artefact caused by spontaneous *Rosa^{YFP}* recombination or unspecific immunostaining, because littermates that did not carry *Csflr-iCre* lacked YFP staining (Fig. 1a). Furthermore, hindbrain imaging from mice carrying *Csflr-iCre* with *CAG-Cat-Egfp* or *Rosa^{tdTom}* as alternative recombination reporters confirmed targeting of both microglia and vessel-bound elongated cells (Extended Data Fig. 1b, c). The tamoxifen-induced activation of CRE, expressed from an independently generated *Csflr-Mer-iCre-Mer* transgene that targets myeloid cells¹⁹, also targeted vessel-bound cells in addition to microglia (Fig. 1d). Corroborating the endothelial identity of *Csflr-iCre*-targeted, elongated vessel-bound cells, these cells expressed the EC markers ERG and PECAM1, had a similar morphology to ECs targeted with the endothelium-specific *Cdh5-CreER^{T2}* transgene, formed junctions with neighbouring ECs via the endothelial cadherin CDH5 and lacked both myeloid and pericyte markers (Fig. 1e, Extended Data Fig. 1d–f).

Csflr-iCre-mediated EC targeting was not explained by *Csflr* expression in brain ECs, because hindbrain ECs, unlike microglia, lacked expression of a *Csflr-Egfp* transgene that faithfully reports *Csflr* promoter activity^{20,21} and accordingly did not contain CSF1R protein

¹UCL Institute of Ophthalmology, University College London, London, UK. ²MRC Centre for Reproductive Health, University of Edinburgh, Edinburgh, UK. ³These authors contributed equally: Alice Plein, Alessandro Fantin. *e-mail: c.ruhrberg@ucl.ac.uk

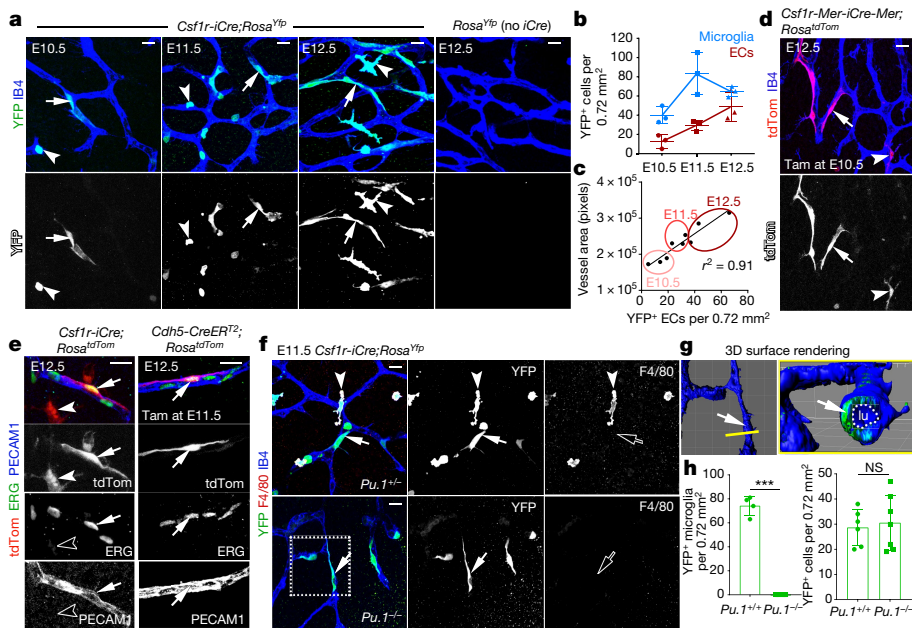


Fig. 1 | *Csf1r-iCre* lineage tracing identifies ECs in developing brain vasculature. **a–c**, Hindbrains of *Csf1r-iCre;Rosa^{Yfp}* mice at the indicated gestational stages. **a**, Whole-mount labelling for YFP and with IB4. **b**, Numbers of YFP⁺IB4⁺ single cells (microglia) and YFP⁺IB4⁺ vessel-bound cells (putative ECs) per 0.72 mm², mean \pm s.d. **c**, Positive correlation between YFP⁺ putative EC number and vessel area (r^2 , coefficient of determination; goodness of fit, $P < 0.01$); each data point represents one hindbrain, $n = 3$ hindbrains for each group. **d, e**, Hindbrains from E12.5 embryos of the indicated genotypes, whole-mount labelled with the indicated markers and shown including tdTomato (tdTom) fluorescence; *Csf1r-Mer-iCre-Mer;Rosa^{tdTom}* (**d**) was tamoxifen-induced on E10.5 and

Cdh5-CreERT2;Rosa^{tdTom} (**e**) on E11.5; $n = 3$ hindbrains for each genotype. **f–h**, Hindbrains from *Csf1r-iCre;Rosa^{Yfp}* embryos on a *Pu.1^{+/+}* versus *Pu.1^{-/-}* background at E11.5, labelled for YFP and F4/80 together with IB4. The boxed area in **f** was 3D surface rendered and is shown in **g** en face and as a lateral view starting at the plane indicated by the yellow line; the vascular lumen (lu) is outlined in the plane. **h**, YFP⁺ microglia (*Pu.1^{+/+}*, $n = 3$) and ECs (*Pu.1^{+/+}*, $n = 6$; *Pu.1^{-/-}*, $n = 7$), mean \pm s.d.; each data point represents one hindbrain; NS, not significant; *** $P < 0.0001$ (two-tailed unpaired *t*-test). Arrowheads, microglia; arrows, ECs. Solid and clear symbols indicate the presence or absence of marker expression, respectively. Scale bars: 20 μ m (**a, d, f**), 50 μ m (**e**).

(Extended Data Fig. 2a, b). Moreover, our analysis of published transcriptomic datasets²² showed that *Csf1r* is not expressed in ECs from embryonic brain, liver or lung, whilst quantitative PCR with reverse transcription (RT-qPCR) analysis of tdTomato⁺ ECs isolated by fluorescence-activated cell sorting (FACS) confirmed that they expressed *Cdh5*, but not *Csf1r* or the myeloid gene *Spi1*, which encodes the PU.1 transcription factor (Extended Data Fig. 2c–g). The lack of endothelial *Csf1r* expression suggests that *Csf1r-iCre*-targeted brain ECs arise from precursors in which *Csf1r* is activated before their incorporation into hindbrain vasculature. These precursors cannot be differentiated myeloid cells such as microglia, whose formation is PU.1-dependent⁴, because PU.1 deficiency did not reduce the number of *Csf1r-iCre*-targeted ECs in the hindbrain at E11.5 (Fig. 1f–h) or the striatum at postnatal day (P)0 (Extended Data Fig. 2h). We therefore investigated whether *Csf1r-iCre*-targeted ECs are derived from PU.1-independent, *Csf1r*-expressing precursors.

Csf1r lineage-traced ECs derive from EMPs

As EMPs are PU.1-independent²³, we investigated whether the formation of *Csf1r-iCre*-targeted ECs was spatiotemporally linked to the emergence of *Csf1r*-expressing EMPs from yolk sac haemogenic endothelium, which was visualized by staining for the EC marker VEGFR2. At E8.5, yolk sacs from *Csf1r-Egfp* embryos contained clusters of round EGFP⁺VEGFR2⁺ cells that protruded from the endothelium into the vascular lumen (Fig. 2a), consistent with previous work showing that FACS-isolated EMPs express both *Csf1r*⁷ and *Vegfr2*⁹, and that EMPs bud from the yolk sac endothelium¹¹. *Csf1r-iCre* lineage tracing in yolk sacs at E8.5 similarly identified round YFP⁺ cells that protruded into the vascular lumen, expressed VEGFR2, persisted in PU.1-deficient yolk sacs and expressed the EMP marker KIT⁷ (Fig. 2b, c; Extended Data Fig. 3a, b). Even though EGFP expression could not be detected in *Csf1r-Egfp* yolk sac endothelium (Fig. 2a), *Csf1r-iCre;Rosa^{Yfp}* also targeted a subset of yolk sac ECs that lacked obvious

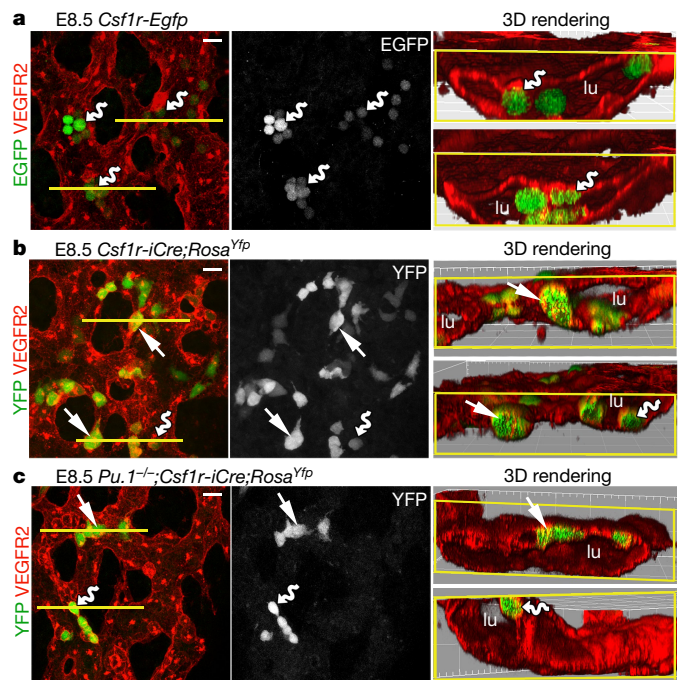


Fig. 2 | *Csf1r-iCre*-targeted ECs emerge concomitantly with EMPs in the yolk sac. E8.5 yolk sacs were whole-mount labelled with the indicated markers. **a**, *Csf1r-Egfp* yolk sacs. **b, c**, *Csf1r-iCre;Rosa^{Yfp}* yolk sacs on a *Pu.1^{+/+}* (**b**) versus *Pu.1^{-/-}* background (**c**). $n = 4$ yolk sacs for each genotype. The yellow lines mark the start of 3D-rendered lateral views. Wavy arrows indicate VEGFR2⁺EGFP⁺ and VEGFR2⁺YFP⁺ round EMPs or myeloid progenitors protruding from the vascular wall into the lumen (lu); straight arrows indicate YFP⁺VEGFR2⁺ flat cells within the vascular wall. Scale bars, 20 μ m.

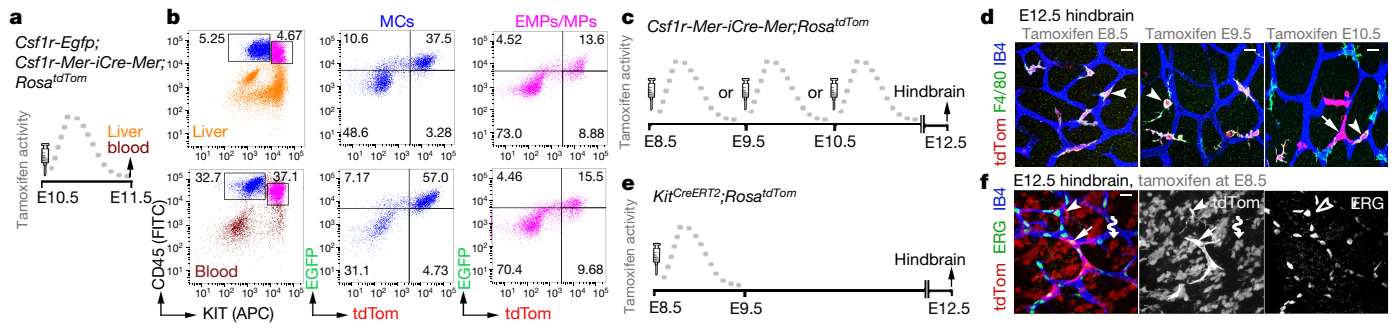


Fig. 3 | *Csf1r-iCre*-targeted hindbrain ECs emerge from intraembryonic EMPs. **a, b,** A pregnant *Csf1r-Egfp; Csf1r-Mer-iCre-Mer; Rosa^{tdTom}* dam was injected with a single dose of tamoxifen on E10.5 (**a**) before FACS of E11.5 liver and blood cells (**b**) to gate the CD45^{high}KIT⁻ differentiated myeloid cell (MCs; blue) and CD45^{low}KIT⁺ EMP/myeloid progenitor (MPs; pink) populations for EGFP and tdTomato ($n = 4$ embryos). **c–f,** Pregnant *Csf1r-Mer-iCre-Mer; Rosa^{tdTom}* (**c, d**) and *Kit^{CreERT2}; Rosa^{tdTom}* (**e, f**) dams

were injected with a single dose of tamoxifen on the indicated days before whole-mount staining of E12.5 hindbrains for the indicated markers and imaging including tdTomato fluorescence; $n = 3$ independent experiments each. Arrows, tdTomato⁺ ECs; arrowheads, microglia; the clear arrowhead indicates lack of ERG expression in microglia; wavy arrows, cluster of tdTomato⁺ERG⁻IB4⁻ neural cells derived from *Kit*⁺ neural progenitors. Scale bars, 20 μ m.

KIT expression (Extended Data Fig. 3b), showing that they were not haemogenic ECs²⁴. Similar to *Csf1r-iCre*-targeted hindbrain ECs, the lineage-traced yolk sac ECs were PU.1-independent (Fig. 2b, c).

The finding that EMP formation correlates with the emergence of *Csf1r-iCre*-targeted yolk sac ECs was corroborated by temporally restricted *Csf1r-Mer-iCre-Mer*-mediated lineage tracing. As tamoxifen-induced, CRE-mediated reporter recombination peaks approximately 6 h and ends 24 h after tamoxifen injection²⁵, we activated *Csf1r-Mer-iCre-Mer; Rosa^{tdTom}* in discrete temporal windows by single injections at E8.5, E9.5 or E10.5 before identifying lineage-traced cells in E12.5 yolk sacs (Extended Data Fig. 3c). Induction at all three stages labelled yolk sac macrophages (Extended Data Fig. 3d), consistent with their origin from *Csf1r*-expressing EMPs⁷ and their maintenance of *Csf1r* expression^{10,12}. In addition, induction at E8.5 or E9.5 yielded

tdTomato⁺ ECs, whereas induction at E10.5 did not (Extended Data Fig. 3d). As EMPs are present in the yolk sac at E8.5 and E9.5, but move to the liver thereafter¹³, their local availability makes them plausible precursors of *Csf1r-iCre*-labelled yolk sac ECs. Consistent with this, tamoxifen induction of a *Kit^{CreERT2}* knock-in allele at E8.5, when KIT⁺ early EMPs are still present in the yolk sac⁷, lineage-traced both yolk sac ECs and macrophages (Extended Data Fig. 3e, f).

In contrast to early wave EMPs that remain in the yolk sac, the late wave EMPs that populate the embryo are reported to lack *Csf1r* expression, at least when they form in the yolk sac⁷. We therefore investigated whether late wave EMPs begin to express *Csf1r* after homing to the liver and whether they are the precursors of the *Csf1r-iCre*-targeted ECs that appear in the hindbrain from E10.5 onwards. Thus, we combined the *Csf1r-Egfp* expression reporter with *Csf1r-Mer-iCre-Mer; Rosa^{tdTom}* and

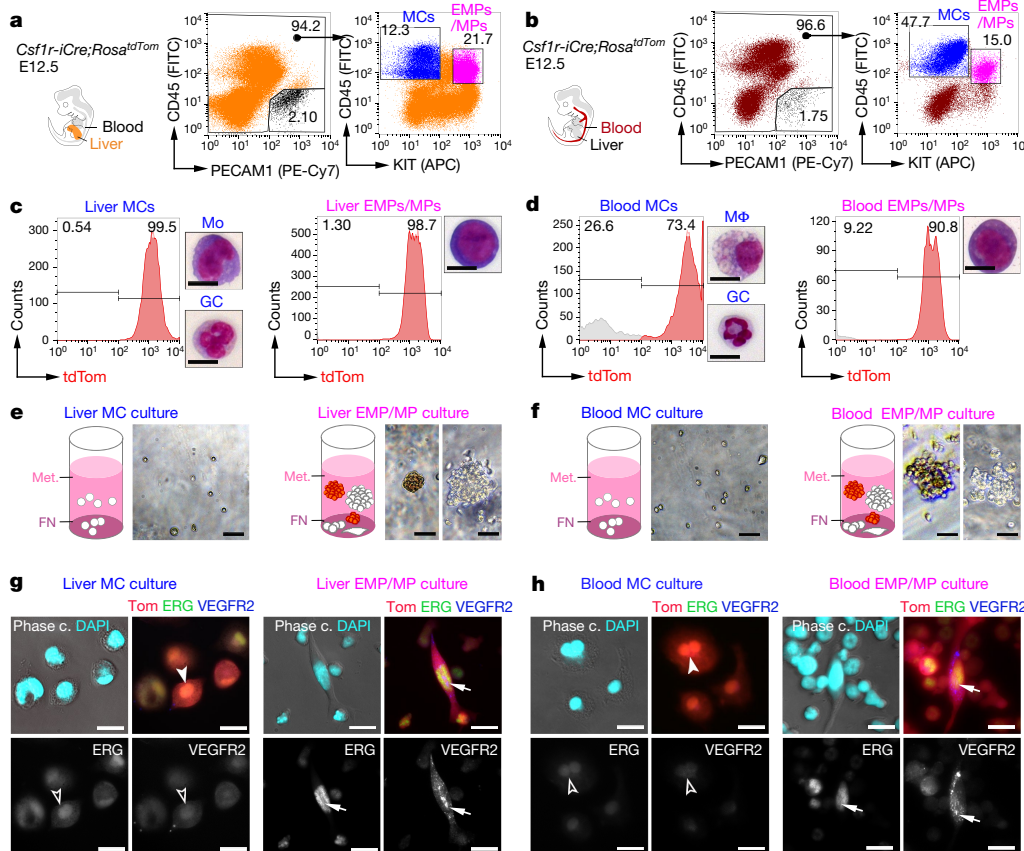


Fig. 4 | EMPs in the liver and blood give rise to ECs in vitro.

a, b, FACS strategy to separate the differentiated myeloid cell and EMP/MP populations from E12.5 *Csf1r-iCre; Rosa^{tdTom}* liver (**a**) and blood (**b**) using antibodies for CD45 and KIT after excluding PECAM1⁺ cells to prevent EC contamination. **c, d,** tdTomato⁺ proportions in the FACS-isolated myeloid cell versus EMP/MP populations from liver and blood shown in **a, b** and Giemsa–Wright staining of representative cells. Mo, monocyte; GC, granulocyte; M ϕ , macrophage. **e–h,** Bright-field images of myeloid (white) and erythroid (rust-coloured) colonies (**e, f**) and immunofluorescence of adherent cells (**g, h**) after three days in methocult (met.) on fibronectin. Adherent cells were immunolabelled for ERG and VEGFR2, counterstained with DAPI and are shown together with tdTomato fluorescence (Tom). Arrows, tdTomato⁺ ECs; arrowheads, tdTomato⁺ myeloid cells; solid and clear symbols indicate high and low marker expression, respectively. Scale bars, 20 μ m. $n = 3$ independent experiments.

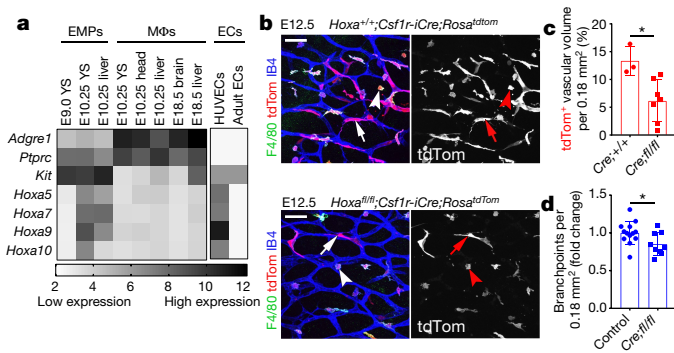


Fig. 5 | *Csf1r-iCre*-targeted ECs form in a *Hoxa*-dependent mechanism and promote vascularization of the embryonic hindbrain.

a, Transcriptomic analysis of the indicated cell populations for the indicated genes, based on published RNA-seq⁹ and microarray data³⁰, shows that *Hoxa* transcripts are enriched in intraembryonic EMPs and perinatal ECs, respectively; white and black represent low and high relative gene expression, respectively; Mφs, macrophages; YS, yolk sac; HUVECs, human umbilical vein ECs; *Adgre1* and *Ptprc* encode F4/80 and CD45, respectively; RNA-seq $n = 2$, except for E10.25 YS (4) and head Mφs (3); microarray $n = 3$. **b–d**, E12.5 littermate hindbrains of the indicated genotypes. **b**, Whole-mount labelling for the indicated markers; RFP staining to visualize tdTomato shows fewer *Csf1r-iCre*-targeted ECs in mutant compared to control hindbrains; arrows, tdTomato⁺ ECs; arrowheads, microglia. Scale bars, 50 μm. **c**, tdTomato⁺ relative to IB4⁺ EC volume in *Hoxa*^{+/+} ($n = 3$) versus *Hoxa*^{fl/fl} ($n = 7$) hindbrains on a *Csf1r-iCre*; *Rosa^{tdTom}* background, mean ± s.d. **d**, SVP complexity, measured as fold change in vascular branchpoints in *Hoxa*^{fl/fl}; *Csf1r-iCre* ($n = 9$) relative to control hindbrains (pooled *Csf1r-iCre*⁺; *Hoxa*^{+/+} and *Csf1r-iCre*⁻ of any *Hoxa* genotype, $n = 13$), mean ± s.d. Each data point represents one hindbrain; * $P = 0.0184$ (c), * $P = 0.0323$ (d) (two-tailed unpaired *t*-test).

induced CRE-mediated recombination at E10.5; 24 h later, we used FACS to separate the differentiated myeloid cells from EMPs and EMP-derived myeloid progenitors⁷ contained in the liver or blood (Fig. 3a, b). The differentiated myeloid cell populations from both sources contained tdTomato⁺EGFP⁺ cells, as expected, but tdTomato⁺EGFP⁺ cells were also present in the EMP/myeloid progenitor populations from both liver and blood (Fig. 3a, b; Extended Data Fig. 3g–i). These findings suggest that a subset of intraembryonic EMPs expresses *Csf1r* and can access organs such as the hindbrain via the circulation.

To determine whether the intraembryonic presence of *Csf1r*-expressing late wave EMPs correlated with the emergence of *Csf1r-iCre*-targeted hindbrain ECs, we visualized tdTomato expression in hindbrains from E12.5 *Csf1r-Mer-iCre-Mer*; *Rosa^{tdTom}* mice after tamoxifen induction at E8.5, E9.5 or E10.5 (Fig. 3c). The hindbrain vasculature contained tdTomato⁺ ECs following induction at E10.5, but not at E8.5 or E9.5, even though the *Csf1r*-expressing microglia were targeted at all stages (Fig. 3d). *Kit^{CreERT2}* induction at E8.5 also caused microglia targeting (Fig. 3e, f), consistent with microglia arising from yolk sac macrophages generated at around E8.5 from KIT⁺ early wave EMPs⁷. Induction of *Kit^{CreERT2}* at E8.5, when late wave EMPs begin to arise in the yolk sac⁷, also yielded tdTomato⁺ ECs in the hindbrain at E12.5 (Fig. 3e, f), confirming that yolk sac-born EMPs can give rise to intraembryonic ECs. Lineage tracing from three independent *Cre* alleles therefore suggests that EMPs give rise to both yolk sac and hindbrain ECs.

Csf1r-expressing EMPs give rise to ECs in vitro

The myeloid and erythroid potential of EMPs has been demonstrated through in vitro differentiation^{11,26}. Using similar assays, we compared the endothelial potential of FACS-isolated differentiated myeloid cell and EMP/myeloid progenitor populations from E12.5 *Csf1r-iCre*; *Rosa^{tdTom}* liver and blood, while ensuring that we were excluding contamination by PECAM1⁺ ECs (Fig. 4a, b). Both cell populations were mostly tdTomato⁺ (Fig. 4c, d). As expected⁷, the EMP-containing

population comprised round cells with a large nucleus and little cytoplasm, whereas the myeloid cell population contained granulocytes, in addition to monocytes in the liver and macrophages in the blood (Fig. 4c, d). For cell culture, we used methocult to promote the formation of haematopoietic colonies, but included a fibronectin substrate to facilitate EC differentiation. Differentiated myeloid cells persisted in these cultures as single round or amoeboid cells (Fig. 4e, f) that were tdTomato⁺ERG^{low}VEGFR2^{low} (Fig. 4g, h; antibody controls in Extended Data Fig. 4a, b). By contrast, both liver and blood EMPs formed myeloid and erythroid cell colonies in suspension (Fig. 4e, f) and additionally gave rise to single adherent cells that appeared spindle-shaped, were tdTomato⁺ERG^{high}VEGFR2^{high} and lacked myeloid cell markers, consistent with an EC identity (Fig. 4g, h; Extended Data Fig. 4c). Together, these experiments demonstrate that EMPs have endothelial potential alongside their known haematopoietic capacity.

Csf1r lineage ECs support blood vessel growth

Hoxa cluster genes modulate haematopoiesis²⁷ and are upregulated in perinatal ECs compared to adult ECs²⁸ (Fig. 5a); HOXA9 also promotes EC differentiation from progenitors in ischaemic disease in adults²⁹. Our analysis of published transcriptomic data^{9,30} revealed that *Hoxa* transcripts are enriched in E10.25 EMPs compared to E9.0 EMPs and macrophages (Fig. 5a). To investigate whether *Hoxa* deficiency impairs the formation of EMP-derived hindbrain ECs, we combined *Csf1r-iCre* with a conditional null *Hoxa* cluster mutation (*Hoxa^{fl/fl}*) (Extended Data Fig. 5a). Gene copy analysis showed effective gene targeting in KIT⁺ cells from *Csf1r-iCre*; *Hoxa^{fl/fl}* mutants at E12.5 compared to control livers, but the number of liver CD45⁺ cells, including differentiated myeloid cells, was not reduced (Extended Data Fig. 5b–f). *Hoxa* genes are therefore dispensable for myeloid cell specification from late wave EMPs. By contrast, fewer tdTomato⁺ ECs, also derived from late wave EMPs, had formed in *Rosa^{tdTom}*-carrying *Csf1r-iCre*; *Hoxa^{fl/fl}* mutant hindbrains compared to control hindbrains; moreover, SVP complexity was reduced in mutant hindbrains (Fig. 5b–d). Although we observed 20% fewer microglia in mutant hindbrains than in control hindbrains (Extended Data Fig. 5g–i), this is not likely to have contributed to the vascular defect, because even a 50% microglia reduction in *Csf1r^{op/+}* mutants did not reduce SVP complexity (Extended Data Fig. 5j–l). Together, these findings suggest that *Hoxa* cluster genes promote the formation of EMP-derived brain ECs, which in turn support normal brain vascular development.

Transcriptional signature of *Csf1r* lineage ECs

Csf1r-iCre-targeted ECs not only appeared morphologically similar to neighbouring ECs (Fig. 1), but also had similarly slow proliferation and overall cell cycle kinetics (Extended Data Fig. 6). Moreover, RNA sequencing (RNA-seq) analysis of FACS-isolated tdTomato⁺ and tdTomato⁻ ECs from E12.5 *Csf1r-iCre*; *Rosa^{tdTom}* embryos showed that they had largely similar transcriptomes, with only a few differentially expressed genes, including the expected difference in the *tdTomato* transcript (Fig. 6a–c; Extended Data Fig. 7a). Corroborating their endothelial identity, tdTomato⁺ ECs lacked markers for differentiated myeloid cells and other non-EC lineages, but expressed core EC transcripts at similar levels to tdTomato⁻ ECs (Fig. 6d, e). Amongst the differentially expressed genes, markers typical of EC specialization, such as ephrins and EPH receptors regulating arteriovenous differentiation, were under-represented in tdTomato⁺ ECs (Fig. 6e). This observation is consistent with *Csf1r-iCre*-targeted ECs being derived from progenitors that are recruited into preformed vascular endothelium. Whereas brain EC markers (for example, *Slc2a1*) were under-represented in the embryo-wide tdTomato⁺ EC population, liver EC markers (for example, *Oit3*, *Mrc1*) were over-represented, including early markers of liver sinusoidal differentiation (*Stab2*, *Lyve1*)³¹ (Fig. 6c, f; Extended Data Fig. 7b, c). Similar expression of *Oit3* and *Mrc1* in tdTomato⁺ and tdTomato⁻ liver ECs (Extended Data Fig. 7d) suggests that the over-representation of liver EC transcripts in the total embryonic tdTomato⁺ EC population reflects their preferential contribution to

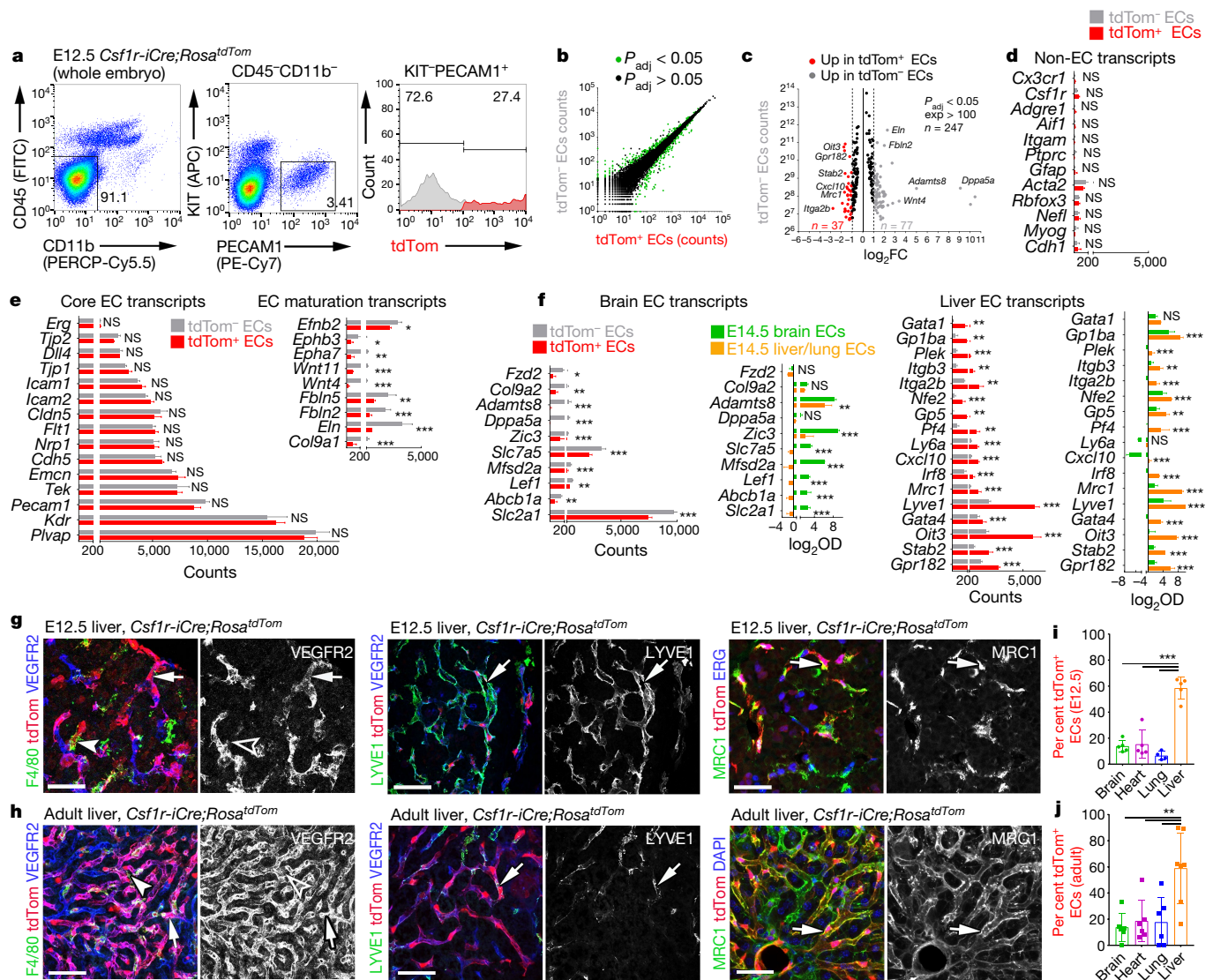


Fig. 6 | The *Csf1r-iCre*-targeted EC population has a core endothelial transcription signature with an increase in liver EC transcripts and persists in adult organs. a–f, Transcriptomic analysis. **a**, FACS strategy to isolate *tdTomato*⁻ and *tdTomato*⁺ ECs from E12.5 *Csf1r-iCre;Rosa^{tdTom}* embryos for RNA-seq. **b**, Graphic representation of genes for which expression was significantly different (green dots) or similar (black dots) between both EC populations. **c**, Volcano plot of significantly differentially expressed transcripts with more than 100 counts per transcript; selected genes are named; grey and red data points represent transcripts in *tdTomato*⁻ ECs with at least twofold over- or under-representation, respectively. **d–f**, Relative expression levels for markers typical of myeloid (*Cx3cr1*–*Ptprc*), astrocytic (*Gfap*), smooth muscle (*Acta2*), neuronal (*Rbfox3*, *Nefl*), skeletal muscle (*Myog*) or epithelial (*Cdh1*) differentiation (**d**), for EC core and maturation markers (**e**) and for representative brain and liver EC specialization markers compared to brain versus liver/lung ECs microarrays³⁰ (**f**); mean \pm s.d.; RNA-seq, $n = 3$ embryos (DESeq2;

Benjamini–Hochberg’s multiple comparisons test for P value adjustment, P_{adj}); microarray, $n = 5$ organs (two-way ANOVA, Bonferroni’s multiple comparisons test); NS, not significant, $*P < 0.05$, $**P < 0.01$, $***P < 0.0001$; see Source Data for exact values. **g, h**, *Csf1r-iCre;Rosa^{tdTom}* E12.5 (**g**) and adult (**h**) liver cryosections, labelled for the indicated markers and RFP to visualize *tdTomato*, including DAPI counterstaining in **h**, $n = 3$ independent experiments. Arrows, *tdTomato*⁺ ECs; arrowheads, macrophages; clear arrowheads indicate that macrophages lack VEGFR2. Scale bar, 50 μ m. **i, j**, FACS of *Csf1r-iCre;Rosa^{tdTom}* E12.5 (**i**) and adult (**j**) brain, heart, lung and liver to determine their relative *tdTomato*⁺ EC contributions; mean \pm s.d.; $n = 5$ organs each (**i**; except lung, $n = 4$), $n = 6$ organs each (**j**; except liver, $n = 7$); each data point represents one organ; $***P < 0.0001$ (**i**); $**P = 0.0023$, 0.0066 , 0.00541 (**j**) for liver versus brain, heart, lung, respectively (one-way ANOVA with Tukey’s multiple comparisons test).

liver vasculature. Immunostaining and FACS of *Csf1r-iCre;Rosa^{tdTom}* E12.5 and E18.5 embryos confirmed that *tdTomato*⁺ ECs were more prevalent than *tdTomato*⁻ ECs in liver endothelium (Fig. 6g; Extended Data Figs. 8, 9a, b). As liver EC specialization markers were present in both *tdTomato*⁻ and *tdTomato*⁺ liver ECs at E12.5 (Fig. 6g; Extended Data Fig. 8a), liver ECs from two distinct origins appear to undergo similar organ-specific EC differentiation.

Csf1r lineage ECs persist in multiple adult organs

Immunostaining and FACS analyses at E12.5 and E18.5 showed that *Csf1r-iCre*-targeted ECs were also present in the heart and lung

vasculature at similar levels to the brain (Fig. 6i; Extended Data Figs. 8, 9a, b). Corresponding immunostaining and FACS analyses showed that *tdTomato*⁺ ECs persisted in the brain, heart, lung and liver of adults and continued to dominate the adult liver sinusoidal endothelium (Fig. 6h, j; Extended Data Figs. 9c, 10a). Accordingly, all adult organs examined contained EMP-derived ECs.

Discussion

The heterogeneous origin of blood vascular mural cells from distinct populations of mesodermal progenitors, haematopoietic and neural crest cells has been established³². Here we have shown that embryonic

vascular endothelium has two major origins. Thus, ECs emerge via a classical pathway of angioblast differentiation into ECs and the pathway described in this report, which entails differentiation of ECs from the EMP lineage (Extended Data Fig. 10b). Multiple previous investigations have used *Csf1r-iCre* together with recombination reporters to follow the embryonic myeloid lineage^{7,10,12}. These studies predominantly used FACS with haematopoietic markers, which precluded observation of *Csf1r-iCre*-targeted ECs. By contrast, we included EC markers in FACS protocols to additionally isolate *Csf1r-iCre*-targeted ECs. In addition, immunostaining was previously used to identify *Csf1r-iCre*-targeted cells in the retina¹⁷, liver and colon¹⁸, but without description of EC targeting, possibly because of the close spatial proximity of ECs and perivascular macrophages^{4,33}. We overcame this limitation by performing high-resolution imaging of tissues immunostained with both EC and myeloid cell markers. The contribution of EMP-derived ECs to the yolk sac, brain, heart and lung vasculature is proportionally smaller than that of ECs of classical origin, whereas EMP-derived ECs predominate in the liver, particularly the sinusoidal endothelium. Liver endothelium was previously reported to be heterogeneous in origin, with an endoderm lineage contribution of approximately 15% and the remainder of the liver EC population attributed to a venous origin³⁴. Our results suggest that liver endothelium contains approximately 60% EMP-derived ECs. Preferential homing of EMPs to the liver after their entry into the embryonic circulation¹³, and the dependence of liver growth on rapid vascular expansion³⁵, may explain the relatively large contribution of EMP-derived ECs to this organ. Ultimately, the discovery that EMPs provide a source of ECs for organ vasculature may open up new therapeutic avenues for vessel-dependent organ repair and regeneration. For example, EMPs or EMP-like EC progenitors, derived from human stem cells by modulating the expression of factors such as *Hoxa* genes, might be delivered systemically to support vascular growth in ischaemic diseases or to provide angiocrine signals that stimulate tissue stem cells.

Online content

Any methods, additional references, Nature Research reporting summaries, source data, statements of data availability and associated accession codes are available at <https://doi.org/10.1038/s41586-018-0552-x>.

Received: 16 December 2016; Accepted: 17 August 2018;

Published online 26 September 2018.

- Potente, M., Gerhardt, H. & Carmeliet, P. Basic and therapeutic aspects of angiogenesis. *Cell* **146**, 873–887 (2011).
- Hirschi, K. K., Ingram, D. A. & Yoder, M. C. Assessing identity, phenotype, and fate of endothelial progenitor cells. *Arterioscler. Thromb. Vasc. Biol.* **28**, 1584–1595 (2008).
- Pollard, J. W. Trophic macrophages in development and disease. *Nat. Rev. Immunol.* **9**, 259–270 (2009).
- Fantin, A. et al. Tissue macrophages act as cellular chaperones for vascular anastomosis downstream of VEGF-mediated endothelial tip cell induction. *Blood* **116**, 829–840 (2010).
- Clausen, B. E., Burkhardt, C., Reith, W., Renkawitz, R. & Förster, I. Conditional gene targeting in macrophages and granulocytes using *LysMcre* mice. *Transgenic Res.* **8**, 265–277 (1999).
- de Boer, J. et al. Transgenic mice with hematopoietic and lymphoid specific expression of *Cre*. *Eur. J. Immunol.* **33**, 314–325 (2003).
- Hoeffel, G. et al. C-Myb⁺ erythro-myeloid progenitor-derived fetal monocytes give rise to adult tissue-resident macrophages. *Immunity* **42**, 665–678 (2015).
- Frame, J. M., McGrath, K. E. & Palis, J. Erythro-myeloid progenitors: “definitive” hematopoiesis in the conceptus prior to the emergence of hematopoietic stem cells. *Blood Cells Mol. Dis.* **51**, 220–225 (2013).
- Mass, E. et al. Specification of tissue-resident macrophages during organogenesis. *Science* **353**, aaf4238 (2016).
- Gomez Pediguero, E. et al. Tissue-resident macrophages originate from yolk-sac-derived erythro-myeloid progenitors. *Nature* **518**, 547–551 (2015).
- McGrath, K. E. et al. Distinct sources of hematopoietic progenitors emerge before HSCs and provide functional blood cells in the mammalian embryo. *Cell Rep.* **11**, 1892–1904 (2015).
- Schulz, C. et al. A lineage of myeloid cells independent of Myb and hematopoietic stem cells. *Science* **336**, 86–90 (2012).
- Ginhoux, F. & Guillemin, M. Tissue-resident macrophage ontogeny and homeostasis. *Immunity* **44**, 439–449 (2016).

- Hoeffel, G. & Ginhoux, F. Fetal monocytes and the origins of tissue-resident macrophages. *Cell. Immunol.* **330**, 5–15 (2018).
- Lux, C. T. et al. All primitive and definitive hematopoietic progenitor cells emerging before E10 in the mouse embryo are products of the yolk sac. *Blood* **111**, 3435–3438 (2008).
- Fantin, A. et al. NRP1 acts cell autonomously in endothelium to promote tip cell function during sprouting angiogenesis. *Blood* **121**, 2352–2362 (2013).
- Stefater, J. A., III et al. Regulation of angiogenesis by a non-canonical Wnt-Flt1 pathway in myeloid cells. *Nature* **474**, 511–515 (2011).
- Deng, L. et al. A novel mouse model of inflammatory bowel disease links mammalian target of rapamycin-dependent hyperproliferation of colonic epithelium to inflammation-associated tumorigenesis. *Am. J. Pathol.* **176**, 952–967 (2010).
- Qian, B. Z. et al. CCL2 recruits inflammatory monocytes to facilitate breast-tumour metastasis. *Nature* **475**, 222–225 (2011).
- Sasmono, R. T. et al. A macrophage colony-stimulating factor receptor-green fluorescent protein transgene is expressed throughout the mononuclear phagocyte system of the mouse. *Blood* **101**, 1155–1163 (2003).
- Burnett, S. H. et al. Conditional macrophage ablation in transgenic mice expressing a Fas-based suicide gene. *J. Leukoc. Biol.* **75**, 612–623 (2004).
- Tam, S. J. et al. Death receptors DR6 and TROY regulate brain vascular development. *Dev. Cell* **22**, 403–417 (2012).
- Kierdorf, K. et al. Microglia emerge from erythromyeloid precursors via Pu.1- and Irf8-dependent pathways. *Nat. Neurosci.* **16**, 273–280 (2013).
- Goldie, L. C., Lucitti, J. L., Dickinson, M. E. & Hirschi, K. K. Cell signaling directing the formation and function of hemogenic endothelium during murine embryogenesis. *Blood* **112**, 3194–3204 (2008).
- Wilson, C. H. et al. The kinetics of ER fusion protein activation *in vivo*. *Oncogene* **33**, 4877–4880 (2014).
- Palis, J., Robertson, S., Kennedy, M., Wall, C. & Keller, G. Development of erythroid and myeloid progenitors in the yolk sac and embryo proper of the mouse. *Development* **126**, 5073–5084 (1999).
- Alharbi, R. A., Pettengell, R., Pandha, H. S. & Morgan, R. The role of *HOX* genes in normal hematopoiesis and acute leukemia. *Leukemia* **27**, 1000–1008 (2013).
- Toshner, M. et al. Transcript analysis reveals a specific *HOX* signature associated with positional identity of human endothelial cells. *PLoS ONE* **9**, e91334 (2014).
- Rössig, L. et al. Histone deacetylase activity is essential for the expression of *HoxA9* and for endothelial commitment of progenitor cells. *J. Exp. Med.* **201**, 1825–1835 (2005).
- Browning, A. C. et al. Comparative gene expression profiling of human umbilical vein endothelial cells and ocular vascular endothelial cells. *Br. J. Ophthalmol.* **96**, 128–132 (2012).
- Nonaka, H., Tanaka, M., Suzuki, K. & Miyajima, A. Development of murine hepatic sinusoidal endothelial cells characterized by the expression of hyaluronan receptors. *Dev. Dyn.* **236**, 2258–2267 (2007).
- Majesky, M. W. Developmental basis of vascular smooth muscle diversity. *Arterioscler. Thromb. Vasc. Biol.* **27**, 1248–1258 (2007).
- Liu, C. et al. Macrophages mediate the repair of brain vascular rupture through direct physical adhesion and mechanical traction. *Immunity* **44**, 1162–1176 (2016).
- Goldman, O. et al. Endoderm generates endothelial cells during liver development. *Stem Cell Reports* **3**, 556–565 (2014).
- Matsumoto, K., Yoshitomi, H., Rossant, J. & Zaret, K. S. Liver organogenesis promoted by endothelial cells prior to vascular function. *Science* **294**, 559–563 (2001).

Acknowledgements We thank the Biological Resources, FACS, Imaging and Genomics facilities at UCL and E. Scarpa for technical help; D. Saur, A. Mass, D. Duboule, M. Kmita and Y. Kubota for mouse strains; and M. Golding for helpful discussions. This research was supported by grants from the Wellcome Trust (095623/Z/11/Z, 101067/Z/13/Z), Medical Research Council (MR/N011511/1) and British Heart Foundation (FS/17/23/32718).

Reviewer information Nature thanks L. Iruela-Arispe and the other anonymous reviewer(s) for their contribution to the peer review of this work.

Author contributions A.P., A.F. and C.R. conceived and planned this study, analysed data and co-wrote the manuscript. L.D. performed genetic crosses and genotyping. A.P. and A.F. either performed experiments together or replicated each other’s experiments, except for the cell cycle and *Hoxa* studies, which were carried out by A.P. and A.F., respectively. J.W.P. provided mouse strains. C.R. supervised the project. All authors reviewed and edited the manuscript.

Competing interests The authors declare no competing interests.

Additional information

Extended data is available for this paper at <https://doi.org/10.1038/s41586-018-0552-x>.

Supplementary information is available for this paper at <https://doi.org/10.1038/s41586-018-0552-x>.

Reprints and permissions information is available at <http://www.nature.com/reprints>.

Correspondence and requests for materials should be addressed to C.R.

Publisher’s note: Springer Nature remains neutral with regard to jurisdictional claims in published maps and institutional affiliations.

METHODS

Mouse strains. All animal procedures were performed in accordance with the institutional Animal Welfare Ethical Review Body (AWERB) and UK Home Office guidelines. To obtain mouse embryos of defined gestational age, mice were paired in the evening and the presence of a vaginal plug the following morning was defined as E0.5. In some studies, we analysed adult mice, defined as more than eight weeks of age. Mice carrying the *Csflr-iCre* transgene¹⁸ were mated to mice carrying the *Cre* recombination reporters *Rosa^{Yfp}* (ref. ³⁶), *Rosa^{tdTom}* (ref. ³⁷) or *CAG-cat-Egfp* (ref. ³⁸). *PU.1^{+/-}* mice³⁹ were mated to *Rosa^{Yfp}* mice and then *Csflr-iCre* mice to obtain *Csflr-iCre;Rosa^{Yfp};Pu.1^{-/-}* embryos that lacked differentiated myeloid cells including microglia^{4,39,40} as well as the myeloid cell precursors of skin pericytes⁴¹. *Hoxa^{fl/fl}* mice⁴² were mated to *Rosa^{tdTom}* mice and then *Csflr-iCre* mice to obtain *Csflr-iCre;Rosa^{tdTom};Hoxa^{fl/fl}* embryos. *Csflr-Mer-iCre-Mer* (ref. ¹⁹) and *Kit^{CREERT2}* (ref. ⁴³) as well as endothelial-specific *Cdh5-Cre-ER^{T2}* (refs. ^{41,44}) mice were mated to *Rosa^{tdTom}* mice. In some experiments, mice carrying the *Csflr-Egfp-Ngfr/Fkbp1a/Tnfrsf6* (short: *Csflr-Egfp*) reporter of *Csflr* expression²¹ were mated to *Csflr-Mer-iCre-Mer;Rosa^{tdTom}* mice. We also used mice with a heterozygous loss of function mutation in *Csfl1* (*Csfl1^{+op}*)⁴⁵. All mouse strains were maintained on a mixed background (C57Bl6/J;129/Sv), with the exception of *Csflr-Mer-iCre-Mer*, which was maintained on a mixed FVB:C57/Bl6 background. For tamoxifen induction of CRE activity, tamoxifen (Sigma) was dissolved in peanut oil and administered via a single intraperitoneal injection into each pregnant dam. For *Csflr-Mer-iCre-Mer* induction, we injected 1 mg tamoxifen; to achieve mosaic *Cdh5-Cre-ER^{T2}* activation, we injected 20 µg tamoxifen; for *Kit^{CREERT2}* induction at E8.5, we injected 3 mg tamoxifen together with 1.75 mg progesterone to increase induction without inducing abortions (Sigma).

Immunolabelling. Samples were fixed in 4% formaldehyde in PBS and processed as whole-mounts or dehydrated in sucrose and embedded in optimal cutting temperature (OCT, Tissue-Tek) compound to cut 20-µm cryosections. Immunolabelling was performed as described previously for whole-mount hindbrains⁴⁶. We used the following antibodies and dilutions: goat anti-CDH5 (1:200; AF1002, lot FQI0116101, R&D Systems), rabbit anti-CSF1R (1:500; sc-692, lot K1212, Santa Cruz), rat anti-EMCN (1:50; sc-65495, lot C2917, Santa Cruz), rabbit anti-ERG (1:200; ab92513, lot GR32027 69-1, Abcam), rat anti-F4/80 (1:500; MCA497R, lot 1605, Serotec), chicken anti-GFP (1:1,000; GFP-1020, lot 0511FP12, Aves) and rabbit anti-GFP (1:500; 598, lot 079, MBL) for YFP or EGFP labelling, rabbit anti-IBA1 (1:500; 019-19741, Wako Chemicals), rat anti-KIT (1:500; 553353, lot 30259, BD Pharmingen), rabbit anti-NG2 (1:200; AB5320, lot 2726769, Millipore), rat anti-PECAM1 (1:200; 553370, lot 5205656, BD Pharmingen), rabbit anti-pHH3 (1:400; 06-570, lot 2825969, Millipore), rabbit anti-RFP (1:1,000; PM005, lot 045, MBL), goat anti-VEGFR2 (1:200; AF644, lot COA0417021, R&D Systems). Secondary antibodies used included Alexa Fluor-conjugated goat anti-chick, -rabbit or -rat IgG (Life Technologies), or, for primary antibodies raised in goat, donkey fluorophore-conjugated FAB fragments of anti-chick, -goat, -rabbit or -rat IgG (Jackson ImmunoResearch). Note that CDH5⁴⁷, ERG⁴⁸, EMCN⁴⁹, PECAM1⁵⁰ and VEGFR2⁵¹ were used as EC markers, whereas F4/80⁵² and IBA1⁵³ were used as macrophage markers and NG2⁵⁴ as a pericyte marker. Biotinylated IB4 (L2140, lot 085M4032V, Sigma) followed by Alexa-conjugated streptavidin (ThermoFisher) was also used to detect brain ECs and microglia^{4,16}. Nuclei were labelled with DAPI. Images were acquired with a LSM710 laser scanning confocal microscope (Zeiss) and processed using LSM image browser (Zeiss) and Photoshop CS4 (Adobe) software. Three-dimensional reconstructions including surface rendering and the generation of virtual slices for lateral views of high-resolution confocal z-stacks was performed using Imaris (Bitplane). Z-stack projections of confocal images are shown unless indicated otherwise in the figure legends.

FACS and cell culture. Tissues were mechanically and enzymatically homogenized in RPMI1640 with 2.5% fetal bovine serum (ThermoFisher), 100 µg/ml collagenase/dispase (Roche), 50 µg/ml DNase (Qiagen) and 100 µg/ml heparin (Sigma), incubated for 5 min with 0.5 mg/ml rat Fc block (Becton Dickinson) and labelled with a combination of PE/Cy7-conjugated rat anti-PECAM1 (clone 390, cat 102418, lot B212262), FITC-conjugated rat anti-CD45 (clone 30-F11, cat 103108, lot B246762) or CD41 (clone MWRReg30, cat 133903, lot B201955), APC-conjugated rat anti-KIT (clone 2B8, cat 105812, lot B217855) and PerCp/Cy5.5-conjugated rat anti-CD11b (clone M1/70, cat 101227) (all BioLegend). Appropriate fluorescence gating parameters were established with unstained tissue, *Csflr-iCre*- or *Csflr-Egfp*-negative tissues and fluorescence-minus-one (FMO) staining. For cell cycle analysis, cell populations were incubated with 10 µg/ml Hoechst 33342 (Sigma) for 30 min at 37 °C⁵⁵ before labelling with PE/Cy7-conjugated rat anti-PECAM1 and performing FACS analysis. In all experiments, doublets were eliminated using pulse geometry gates (FSC-H versus FSC-A and SSC-H versus SSC-A), whereas dead cells were removed using SYTOX Blue (Life Technologies) or LIVE/DEAD Fixable Violet (Life Technologies). Single-cell suspensions were analysed using the BD LSRFortessa X-20 cell analyser or sorted using the BD Influx cell sorter (BD Biosciences); FlowJo software (FlowJo LLC) was

used for subsequent analyses. In some experiments, a fraction of each population was cytospun onto a glass slide for Wright–Giemsa staining (Sigma) followed by imaging using an LSM510 microscope equipped with an AxioCam MRc camera (Zeiss). For cell culture experiments, cell populations were sorted into DMEM with 100 U/ml penicillin, 100 U/ml streptomycin and 20% fetal bovine serum (all ThermoFisher) before seeding the cells into a 96-well plate coated with 10 µg/ml fibronectin (ThermoFisher) to facilitate EC differentiation. Cells were then cultured in methocult (STEMCELL Technologies) to promote the formation of haematopoietic colonies, which were imaged using a TS100 microscope equipped with a DS-5M colour camera (Nikon). After removal of methocult, adherent cells were fixed with 4% formaldehyde in PBS and then labelled for VEGFR2, ERG, CD45, F4/80 and CSF1R (see above) before imaging using a Ti-E microscope (Nikon).

RNA-seq. PECAM1⁺CD45⁻CD11b⁻KIT⁻ ECs were isolated from E12.5 *Csflr-iCre;Rosa^{tdTom}* embryos and divided into tdTomato⁺ and tdTomato⁻ populations with the BD Influx cell sorter before RNA was extracted with the RNeasy Micro Kit (QIAGEN). cDNA was generated and amplified using the SMART-seq V4 ultra low input RNA kit (Clontech). 100 pg of amplified cDNA per sample was used to prepare a library with the Nextera XT kit (Illumina) and run on the NextSeq 500 sequencer (Illumina). Raw sequence data were pre-processed to trim poor quality base calls and adaptor contamination using Trimmomatic v.0.36.4⁵⁶ and aligned to the mouse mm10 genome with STAR v.2.5.2b⁵⁷. Mapped reads were deduplicated to reduce PCR bias using Picard v2.7.1.1 software (<http://broadinstitute.github.io/picard/>), and the reads-per-transcript were then calculated using FeatureCount v1.4.6.p5 software⁵⁸. Differential expression was performed using the BioConductor package DESeq2 via the SARTools wrapper v1.3.2.0⁵⁹.

RT-PCR. We extracted RNA from cells isolated with the BD Influx cell sorter (see above) with the RNeasy Micro Kit for cDNA synthesis with Superscript IV (ThermoFisher). Quantitative (q)RT-PCR was performed with SYBR Green on an HT7900 system (Applied Biosystems) using the following oligonucleotide pairs: *Actb* 5'-CACACACCTTCTACAATGAG-3' and 5'-GTCTCAAACATGATCTGGGTC-3'; *Cdh5* 5'-GATGCAGATGACCCCACTGT-3' and 5'-AGGGCATCTGTGTTCCAC-3'; *Csflr* 5'-TGCGTCTACACAGTTCAGAG-3' and 5'-ATGCTGTGATGTTCTTCGGT-3'; *Spi1* 5'-GCCATAGCAGTACTACTG-3' and 5'-CAAGGTTTGATAAGGGAAGC-3'; *Hoxa11* 5'-TCTTTGCTCTCTCCTCTCTT-3' and 5'-TTGCAGACGCTTCTCTTTGTT-3'; *Evx1* 5'-GTGTGCTCTGGGCTCCTGT-3' and 5'-GCCAGGGTGCCTTGAGAG-3; *Slc2a1* 5'-CCCCAGAAGTTATTGAGGAGT and 5'-ACAAAGAGGCCGACAGAGAA; *Mrc1* 5'-ACTGGCAATGCAAATGGAG and 5'-CCCTCAAAGTGCAA TGGACA; *Oit3* 5'-CGTCTGCTCCATGTCTACTG and 5'-GTGCTCACATTC ATTTTCGTGA. For each oligonucleotide pair, a no-template control reaction was included.

Microarray analysis. Published microarray data were used to compare gene expression levels (normalized log₂ OD) in E14.5 CD45⁻PECAM1⁺ brain versus pooled lung and liver ECs (GSE35802)²² and in HUVECs versus adult retinal ECs (GSE20986)³⁰ using GEO2R software (NCBI).

Statistical analysis. No randomization method was used, because tissues for analysis were allocated to experimental groups according to genotype, gestational age, organ or cell type. To ensure unbiased interpretation of results, the genotype and gestational age were disclosed only after data collection was complete, but the investigators were not blinded to sample origin (organ or cell type). All experiments involving two or more genotypes for comparison included littermate controls, and the minimum sample number was three. No statistical methods were used to predetermine sample size. The number of YFP⁺ ECs and YFP⁺ microglia in *Csflr-iCre;Rosa^{Yfp}* hindbrains (Fig. 1a, b, f–h) was determined in three randomly chosen 0.72-mm² regions of each whole-mount labelled and flat-mounted hindbrain. For hindbrains in *Hoxa*-targeting experiments, the number of F4/80⁺ microglia (Extended Data Fig. 5) and tdTomato⁺ and IBA4⁺ volume (Fig. 5b, c) were determined from confocal z-stacks of four randomly chosen 0.18-mm² regions on the lateral side of each hindbrain (Extended Data Fig. 5g). The z-stacks were surface rendered with Imaris (Bitplane) to obtain the F4/80⁺ and IBA4⁺ volumes, and the F4/80⁺ volume was then subtracted from both the IBA4⁺ and tdTomato⁺ total volumes to obtain the IBA4⁺ EC and tdTomato⁺ EC volumes before calculating the ratio of tdTomato⁺ to IBA4⁺ EC volume. To determine the number of vascular intersections in *Hoxa*-targeting experiments (Fig. 5b,d), the same confocal z-stacks were analysed with Imaris filament tracer after F4/80⁺ microglia were masked. For Figs. 1, 5, all counts obtained from one hindbrain were averaged to yield the value for that hindbrain. For all experiments, we calculated the mean value for at least three independent samples, where error bars represent the standard deviation of the mean (for details, see legends). Comparison of medians against means justified the use of a parametric test; to determine whether two datasets were significantly different, we therefore calculated *P* values with a two-tailed unpaired Student's *t*-test; *P* < 0.05 was considered significant. When more than two datasets were compared, we used the statistical tests indicated in the associated legends.

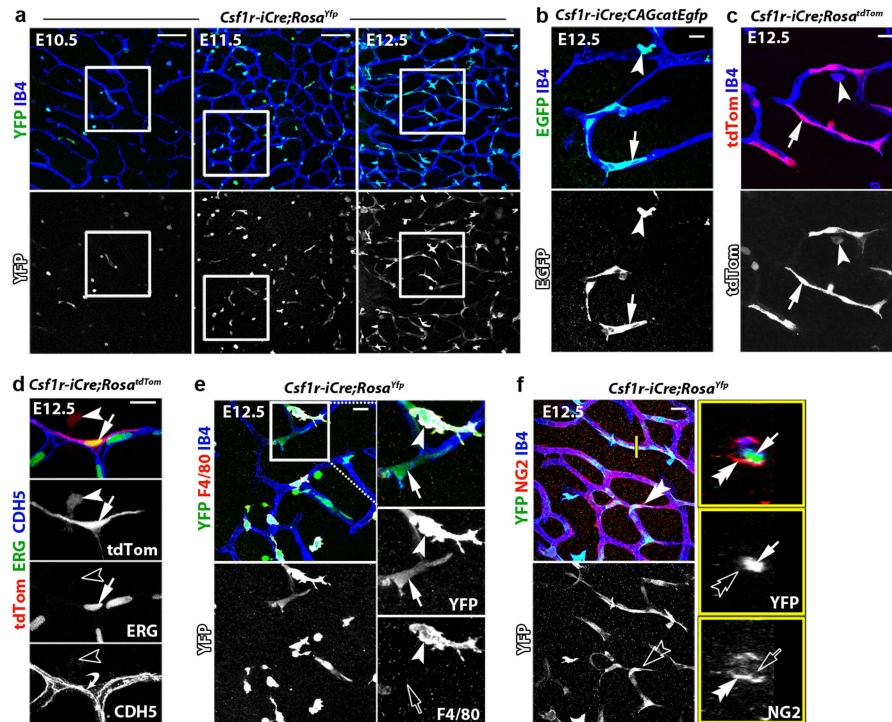
Statistical analyses were performed with Excel 12.2.6 (Microsoft Office) or Prism 7 (GraphPad Software).

Reporting summary. Further information on experimental design is available in the Nature Research Reporting Summary linked to this paper.

Data availability

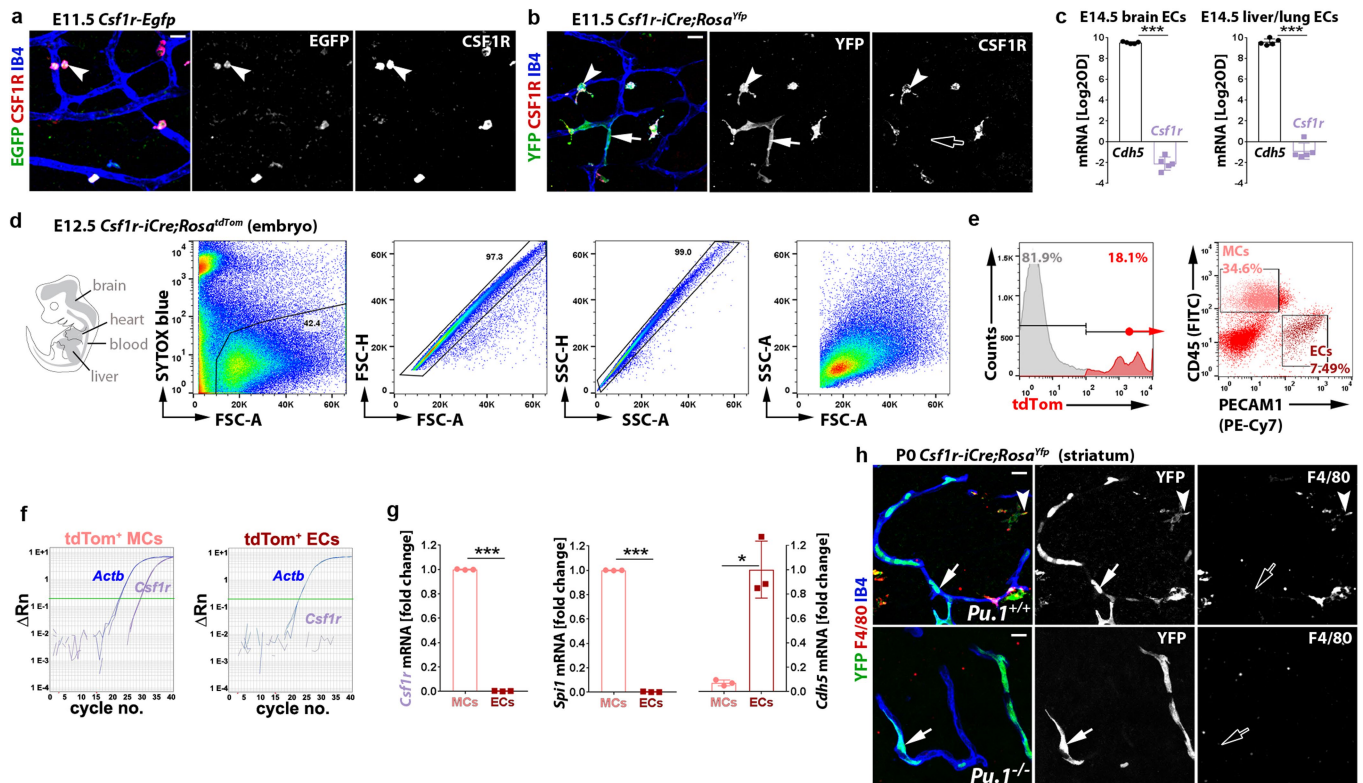
All sequence data used in this study have been deposited in the NCBI Gene Expression Omnibus database (accession number GSE117978) and are listed in the Source Data for Fig. 6.

36. Srinivas, S. et al. Cre reporter strains produced by targeted insertion of *EYFP* and *ECFP* into the *ROSA26* locus. *BMC Dev. Biol.* **1**, 4 (2001).
37. Madisen, L. et al. A robust and high-throughput Cre reporting and characterization system for the whole mouse brain. *Nat. Neurosci.* **13**, 133–140 (2010).
38. Kawamoto, S. et al. A novel reporter mouse strain that expresses enhanced green fluorescent protein upon Cre-mediated recombination. *FEBS Lett.* **470**, 263–268 (2000).
39. McKercher, S. R. et al. Targeted disruption of the PU.1 gene results in multiple hematopoietic abnormalities. *EMBO J.* **15**, 5647–5658 (1996).
40. Scott, E. W., Simon, M. C., Anastasi, J. & Singh, H. Requirement of transcription factor PU.1 in the development of multiple hematopoietic lineages. *Science* **265**, 1573–1577 (1994).
41. Yamazaki, T. et al. Tissue myeloid progenitors differentiate into pericytes through TGF- β signaling in developing skin vasculature. *Cell Rep.* **18**, 2991–3004 (2017).
42. Kmita, M. et al. Early developmental arrest of mammalian limbs lacking *HoxA/HoxD* gene function. *Nature* **435**, 1113–1116 (2005).
43. Klein, S. et al. Interstitial cells of Cajal integrate excitatory and inhibitory neurotransmission with intestinal slow-wave activity. *Nat. Commun.* **4**, 1630 (2013).
44. Zarkada, G., Heinolainen, K., Makinen, T., Kubota, Y. & Alitalo, K. VEGFR3 does not sustain retinal angiogenesis without VEGFR2. *Proc. Natl Acad. Sci. USA* **112**, 761–766 (2015).
45. Yoshida, H. et al. The murine mutation osteopetrosis is in the coding region of the macrophage colony stimulating factor gene. *Nature* **345**, 442–444 (1990).
46. Fantin, A., Vieira, J. M., Plein, A., Maden, C. H. & Ruhrberg, C. The embryonic mouse hindbrain as a qualitative and quantitative model for studying the molecular and cellular mechanisms of angiogenesis. *Nat. Protoc.* **8**, 418–429 (2013).
47. Gory-Fauré, S. et al. Role of vascular endothelial-cadherin in vascular morphogenesis. *Development* **126**, 2093–2102 (1999).
48. McLaughlin, F., Ludbrook, V. J., Kola, I., Campbell, C. J. & Randi, A. M. Characterisation of the tumour necrosis factor (TNF)-(α) response elements in the human ICAM-2 promoter. *J. Cell Sci.* **112**, 4695–4703 (1999).
49. Morgan, S. M., Samulowitz, U., Darley, L., Simmons, D. L. & Vestweber, D. Biochemical characterization and molecular cloning of a novel endothelial-specific sialomucin. *Blood* **93**, 165–175 (1999).
50. Albelda, S. M., Muller, W. A., Buck, C. A. & Newman, P. J. Molecular and cellular properties of PECAM-1 (endoCAM/CD31): a novel vascular cell-cell adhesion molecule. *J. Cell Biol.* **114**, 1059–1068 (1991).
51. Shalaby, F. et al. Failure of blood-island formation and vasculogenesis in Flk-1-deficient mice. *Nature* **376**, 62–66 (1995).
52. Austyn, J. M. & Gordon, S. F4/80, a monoclonal antibody directed specifically against the mouse macrophage. *Eur. J. Immunol.* **11**, 805–815 (1981).
53. Ohsawa, K., Imai, Y., Sasaki, Y. & Kohsaka, S. Microglia/macrophage-specific protein Iba1 binds to fimbria and enhances its actin-bundling activity. *J. Neurochem.* **88**, 844–856 (2004).
54. Ozerdem, U., Grako, K. A., Dahlin-Huppe, K., Monosov, E. & Stallcup, W. B. NG2 proteoglycan is expressed exclusively by mural cells during vascular morphogenesis. *Dev. Dyn.* **222**, 218–227 (2001).
55. Goodell, M. A., Brose, K., Paradis, G., Conner, A. S. & Mulligan, R. C. Isolation and functional properties of murine hematopoietic stem cells that are replicating in vivo. *J. Exp. Med.* **183**, 1797–1806 (1996).
56. Bolger, A. M., Lohse, M. & Usadel, B. Trimmomatic: a flexible trimmer for Illumina sequence data. *Bioinformatics* **30**, 2114–2120 (2014).
57. Dobin, A. et al. STAR: ultrafast universal RNA-seq aligner. *Bioinformatics* **29**, 15–21 (2013).
58. Liao, Y., Smyth, G. K. & Shi, W. featureCounts: an efficient general purpose program for assigning sequence reads to genomic features. *Bioinformatics* **30**, 923–930 (2014).
59. Varet, H., Brillet-Guéguen, L., Coppée, J. Y. & Dillies, M. A. SARTools: A DESeq2- and EdgeR-based R pipeline for comprehensive differential analysis of RNA-seq data. *PLoS ONE* **11**, e0157022 (2016).



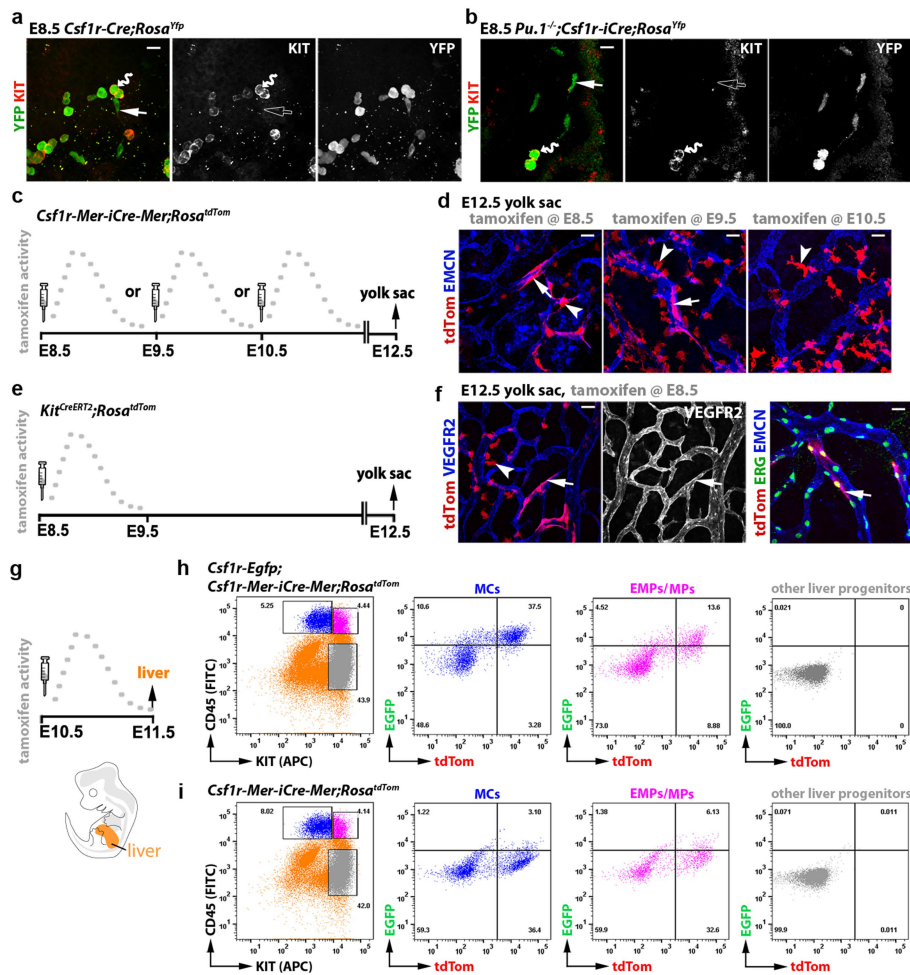
Extended Data Fig. 1 | Endothelial *Csfl1r-iCre*-targeting is observed with different recombination reporters, and targeted ECs are distinguishable from macrophages and pericytes. a–c, *Csfl1r-iCre;Rosa^{Yfp}* (a), *Csfl1r-iCre;CAG-Cat-Egfp* (b) and *Csfl1r-iCre;Rosa^{tdTom}* (c) hindbrains ($n = 3$ each) at the indicated stages were whole-mount labelled with IB4 and for YFP (a) or GFP (b) or are shown with tdTomato fluorescence (c). In a, the white squares indicate areas that were imaged at higher magnification for Fig. 1a. The indicated single channels are also shown individually. d, *Csfl1r-iCre;Rosa^{tdTom}* E12.5 hindbrains ($n = 3$), whole-mount labelled for ERG and CDH5 and shown including tdTomato fluorescence to demonstrate that *Csfl1r-iCre* targets ECs that form junctions with neighbouring

non-targeted ECs. e, f, E12.5 *Csfl1r-iCre;Rosa^{Yfp}* hindbrains, labelled for YFP and the microglia marker F4/80 (e) or the pericyte marker NG2 (f) together with IB4, show that *Csfl1r-iCre*-targeted vessel-bound cells are neither microglia nor pericytes; $n = 3$ each. In e, the boxed area is shown in higher magnification and as single channels adjacent to the panel. In f, a single optical y/z cross section at the position indicated with the yellow line is displayed at higher magnification with single channels. Arrowheads, microglia; arrows, ECs; double arrowheads, pericytes; curved arrow, junctional CDH5 staining; solid and clear symbols indicate the presence or absence of marker expression, respectively. Scale bars: 100 μm (a), 20 μm (b, c, e, f), 50 μm (d).



Extended Data Fig. 2 | Endothelial *Csf1r-iCre*-targeting is not caused by endothelial *Csf1r* expression and occurs independently of myeloid differentiation. **a, b**, *Csf1r-Egfp* (**a**) and *Csf1r-iCre;Rosa^{Yfp}* (**b**) E11.5 hindbrains ($n = 3$ each), whole-mount labelled for CSF1R and EGFP or YFP together with IB4, show lack of *Csf1r* promoter activity and CSF1R protein in ECs. **c**, Relative *Cdh5* and *Csf1r* expression levels in our analysis of published E14.5 brain or pooled lung/liver EC microarrays²², $n = 5$ each; $***P < 0.0001$ (two-tailed unpaired *t*-test). **d–g**, FACS separation of tdTomato⁺ cells from *Csf1r-iCre;Rosa^{tdTom}* embryos ($n = 3$) for gene expression analysis, including representative gating strategy to exclude dead cells and doublets in this and subsequent experiments (**d**) and sorting into PECAM1⁺CD45⁻ ECs versus CD45⁺PECAM1⁻ MCs (**e**).

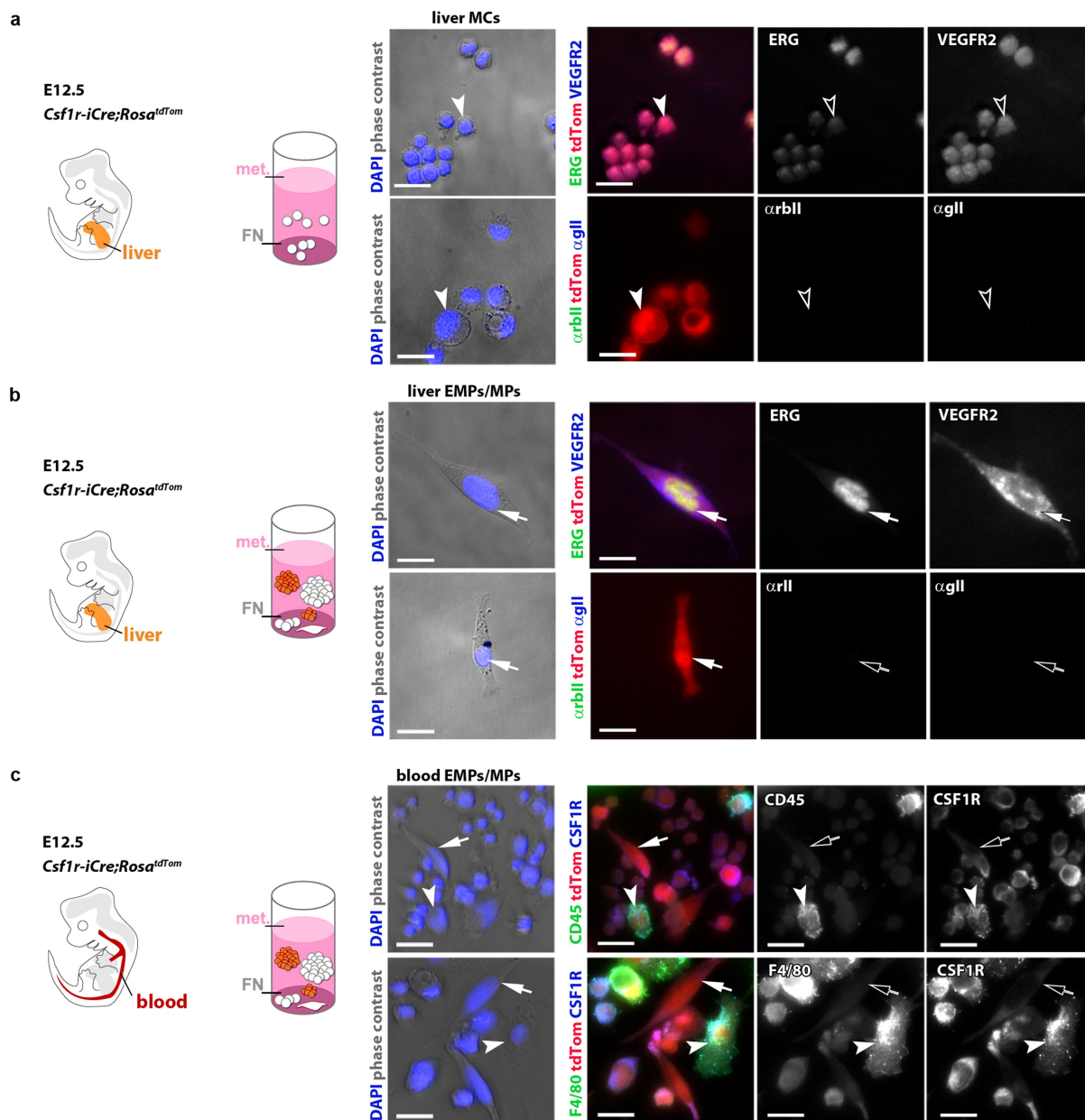
f, Representative RT–qPCR gene amplification graphs for *Csf1r* and *Actb* from tdTomato⁺ MCs and ECs; ΔRn , normalized reporter value for SYBR Green minus baseline instrument signals. **g**, Graphic representation of the fold change in RT–qPCR amplification of the indicated genes relative to *Actb* for both cell populations; each data point represents one embryo; $*P = 0.0242$, $***P < 0.0001$ (two-tailed unpaired *t*-test). **h**, *Csf1r-iCre;Rosa^{Yfp}* P0 striatum on a *Pu.1^{+/+}* versus *Pu.1^{-/-}* background ($n = 3$ brains each), cryosectioned and labelled for YFP and F4/80 together with IB4 to show that *Csf1r-iCre*-targeted ECs are PU.1-independent and persist postnatally. Arrowheads, microglia; arrows, YFP⁺ ECs; clear arrows, YFP⁺ ECs that are CSF1R⁻ and F4/80⁻. Scale bars, 20 μ m.



Extended Data Fig. 3 | Lineage tracing of yolk sac and liver EMPs.

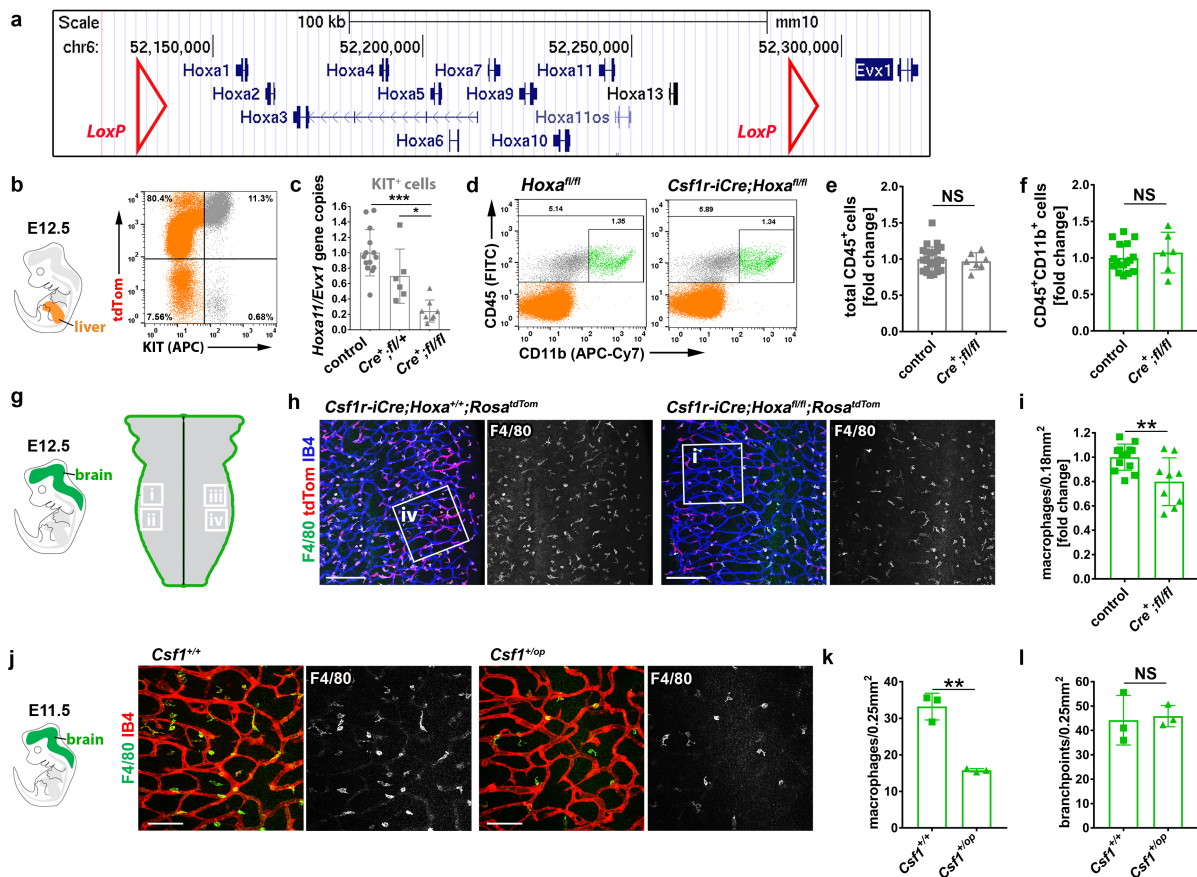
a, b, E8.5 wild-type (**a**) and *Pu.1^{-/-}* (**b**) yolk sacs on a *Csf1r-iCre;Rosa^{Yfp}* background ($n = 3$ yolk sacs each), whole-mount labelled for YFP and KIT, show *Csf1r-iCre*-targeted KIT⁺ round cells corresponding to EMPs and MPs as well as *Csf1r-iCre*-targeted KIT⁻ flat cells corresponding to ECs. Scale bars, 20 μm . **c–f**, Pregnant *Csf1r-Mer-iCre-Mer;Rosa^{tdTom}* (**c, d**) and *Kit^{CreERT2};Rosa^{tdTom}* (**e, f**) dams were injected with a single tamoxifen dose on the indicated days; E12.5 yolk sacs were whole-mount labelled for the indicated markers to identify *Csf1r-iCre*-targeted ECs and macrophages ($n = 3$ yolk sacs for each genotype). Wavy arrows, EMPs; straight arrows,

Csf1r-iCre-lineage-traced ECs; arrowheads, macrophages; solid and clear symbols indicate the presence or absence, respectively, of the indicated markers. Scale bars, 20 μm . **g–i**, Pregnant dams were injected with a single tamoxifen dose on E10.5 (**g**) before using the indicated markers for FACS analysis of E11.5 *Csf1r-Egfp;Csf1r-Mer-iCre-Mer;Rosa^{tdTom}* (**h**) or *Csf1r-Mer-iCre-Mer;Rosa^{tdTom}* control (**i**) livers ($n = 4$ each); the CD45^{high}KIT⁻ differentiated MC (blue), CD45^{low}KIT⁺ EMP/MP (pink) and CD45⁻KIT⁺ (grey) populations were gated further for *Csf1r-Egfp* and tdTomato. CD45⁻KIT⁺ cells were neither MCs nor EMPs, because they lacked CD45, tdTomato and EGFP.



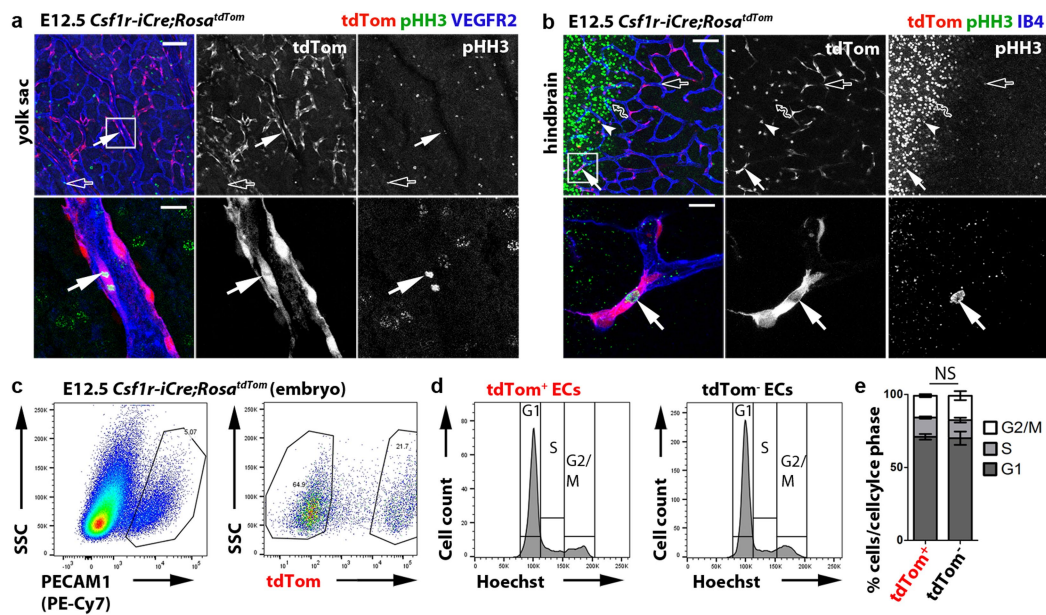
Extended Data Fig. 4 | Immunostaining controls for cultured *Csf1r-iCre*-targeted cells. The indicated cell populations were FACS-isolated from E12.5 *Csf1r-iCre;Rosa^{tdTom}* liver or blood with the indicated markers and cultured for three days in methocult (met.) on fibronectin (FN); $n = 1$ experiment. **a, b**, Adherent cells from tdTomato⁺ liver MC (**a**) and EMP/MP (**b**) cultures were stained for ERG and VEGFR2 (top) or with secondary antibodies only (bottom). **c**, Adherent cells from tdTomato⁺ blood EMP and MP cultures were immunostained for CSF1R together

with the myeloid markers CD45 (top) or F4/80 (bottom). In the first panel in each row, the phase contrast and DAPI images were merged. In panels 2–4 in each row, immunolabelled cells were visualized together with tdTomato fluorescence, with single channels for the indicated markers shown separately in greyscale. Arrows, tdTomato⁺ ECs; arrowheads, tdTomato⁺ MCs; solid and clear symbols indicate the presence or absence, respectively, of the indicated markers. Scale bars, 20 μ m.



Extended Data Fig. 5 | *Hoxa* gene targeting with *Csf1r-iCre*. **a**, Schematic representation of the *Hoxa* gene cluster and adjacent *Evx1* gene using the UCSC Genome Browser with the mouse December 2011 (GRCm38/mm10) Assembly, including position of the *LoxP* sites used for gene targeting. **b**, **c**, Validation of *Hoxa* targeting. **b**, FACS strategy to isolate *KIT*⁺ cells from E12.5 control (pooled *Csf1r-iCre*⁻ or *Csf1r-iCre*⁺; *Hoxa*^{+/+}; *n* = 14), *Hoxa*^{+/fl}; *Csf1r-iCre* (*n* = 6) and *Hoxa*^{fl/fl}; *Csf1r-iCre* (*n* = 8) livers. **c**, qPCR analysis of *Hoxa11* gene copy number relative to *Evx1*; mean ± s.d.; each symbol represents the value for one liver; **P* = 0.0156, ****P* < 0.001 (one-way ANOVA, Tukey's multiple comparisons test). **d–f**, Representative FACS analysis (**d**) and quantification (**e**, **f**) of liver cell populations at E12.5 shows a similar number of total *CD45*⁺ and *CD45*⁺*CD11b*⁺ differentiated myeloid cells in *Hoxa*^{fl/fl}; *Csf1r-iCre* mutants (*n* = 7 for *CD45*⁺; *n* = 6 for *CD45*⁺*CD11b*⁺) versus pooled *Csf1r-iCre*⁻ and *Csf1r-iCre*⁺; *Hoxa*^{+/+} controls (*n* = 25 for *CD45*⁺, *n* = 17 for *CD45*⁺*CD11b*⁺); mean ± s.d. fold change in mutants compared to controls; each data point represents one liver; NS, not significant, *P* = 0.6519 (**e**) and *P* = 0.496 (**f**) (two-tailed unpaired *t*-test). **g–i**, E12.5 hindbrains of the indicated genotypes were immunolabelled

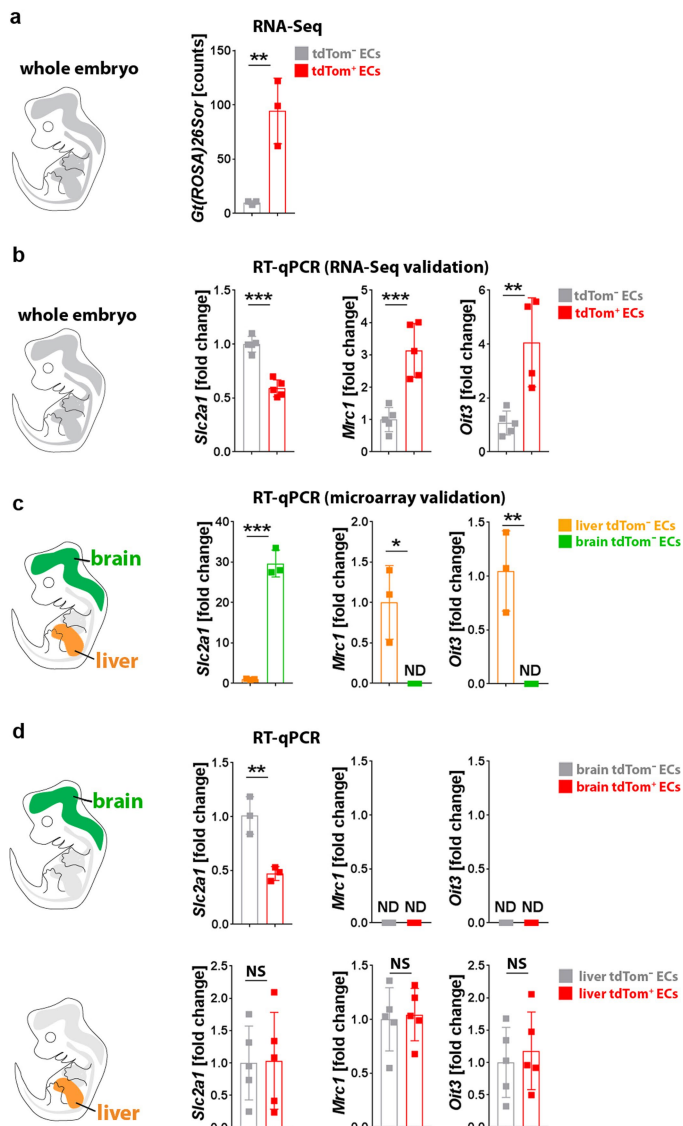
to determine vascular complexity and quantify microglia. **g**, Schematic representation of a whole-mount embryonic hindbrain (left) and location of the hindbrain areas i–iv used for quantification (right); values for the four areas in each hindbrain were averaged to obtain the value for that hindbrain; EC quantifications are shown in Fig. 5c. **h**, Hindbrains were whole-mount labelled with IB4 and for RFP to visualize *tdTomato* and for F4/80 to visualize microglia; white boxes indicate areas shown in higher magnification in Fig. 5. **i**, Quantification of microglia in *Hoxa*^{*fl/fl*}; *Csf1r-iCre* mutants (*n* = 9) versus controls (*n* = 10, pooled *Csf1r-iCre*⁺; *Hoxa*^{+/+} and *Csf1r-iCre*⁻ of any *Hoxa* genotype); mean ± s.d. fold change in mutant compared to control hindbrain; each data point represents one hindbrain; ***P* = 0.0055 (two-tailed unpaired *t*-test). **j–l**, E11.5 *Csf1*^{+/+} and *Csf1*^{+/op} littermate hindbrains, whole-mount labelled for F4/80 together with IB4 (**j**) before quantification of microglia number (**k**) and vascular branchpoints as a measure of vascular complexity (**l**). Mean ± s.d.; each data point represents one hindbrain, *n* = 3 each; NS, not significant, *P* = 0.808, ***P* = 0.0012 (two-tailed unpaired *t*-test). Scale bars: 200 μm (**h**), 100 μm (**j**).



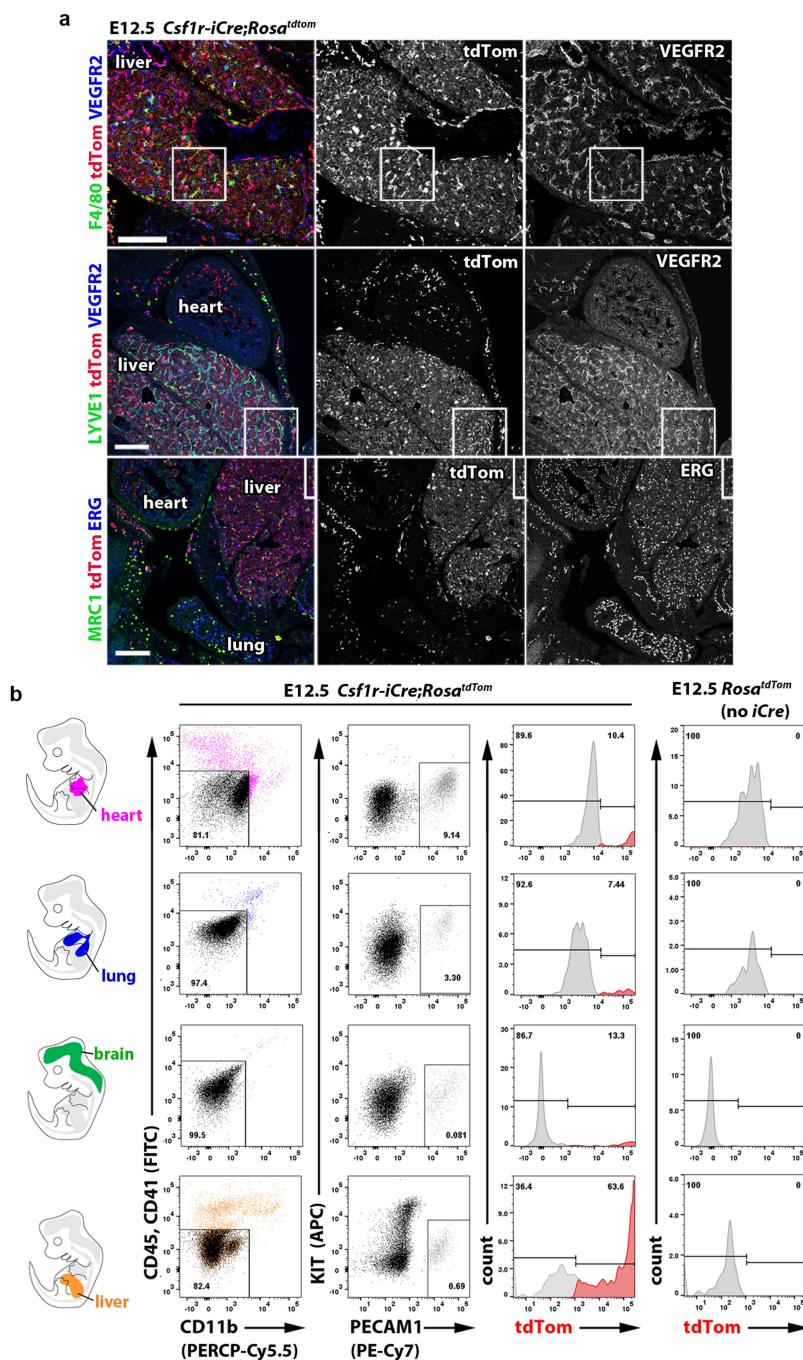
Extended Data Fig. 6 | *Csf1r-iCre*-targeted ECs proliferate in vivo.

a, b, E12.5 *Csf1r-iCre;Rosa^{tdTom}* yolk sac (**a**) or hindbrain (**b**), whole-mount stained for the proliferation marker pHH3 and VEGFR2 or for pHH3 together with IB4, respectively, and shown together with tdTomato fluorescence ($n = 3$ each). Areas indicated with white squares were imaged at higher magnification and are shown below the corresponding panels, with tdTomato and pHH3 channels also shown separately in greyscale. Arrows, proliferating tdTomato⁺pHH3⁺ ECs; solid and clear symbols indicate the presence or absence, respectively, of tdTomato fluorescence; wavy arrow, a tdTomato⁻pHH3⁺ neural progenitor. Scale bars: 100 μm (top), 20 μm (bottom). **c–e**, Cell cycle distribution of

tdTomato⁺ and tdTomato⁻ ECs. **c**, FACS strategy to isolate tdTomato⁺ and tdTomato⁻PECAM1⁺ ECs from E12.5 *Csf1r-iCre;Rosa^{tdTom}* embryos ($n = 3$ embryos). **d**, Cell cycle distribution based on Hoechst 33342 fluorescence as a measure of DNA content; low and high staining intensity is observed in cells with a DNA ploidy of $2n$ (G0/G1 phase) or $4n$ (G2/M phase), respectively; intermediate staining intensity corresponds to S phase. **e**, Mean \pm s.d. proportion of tdTomato⁺ and tdTomato⁻ ECs in G1, S and G2/M based on the area of the corresponding peaks in **d**; NS, not significant, $P > 0.9999$ (two-way ANOVA, Bonferroni's multiple comparisons test).

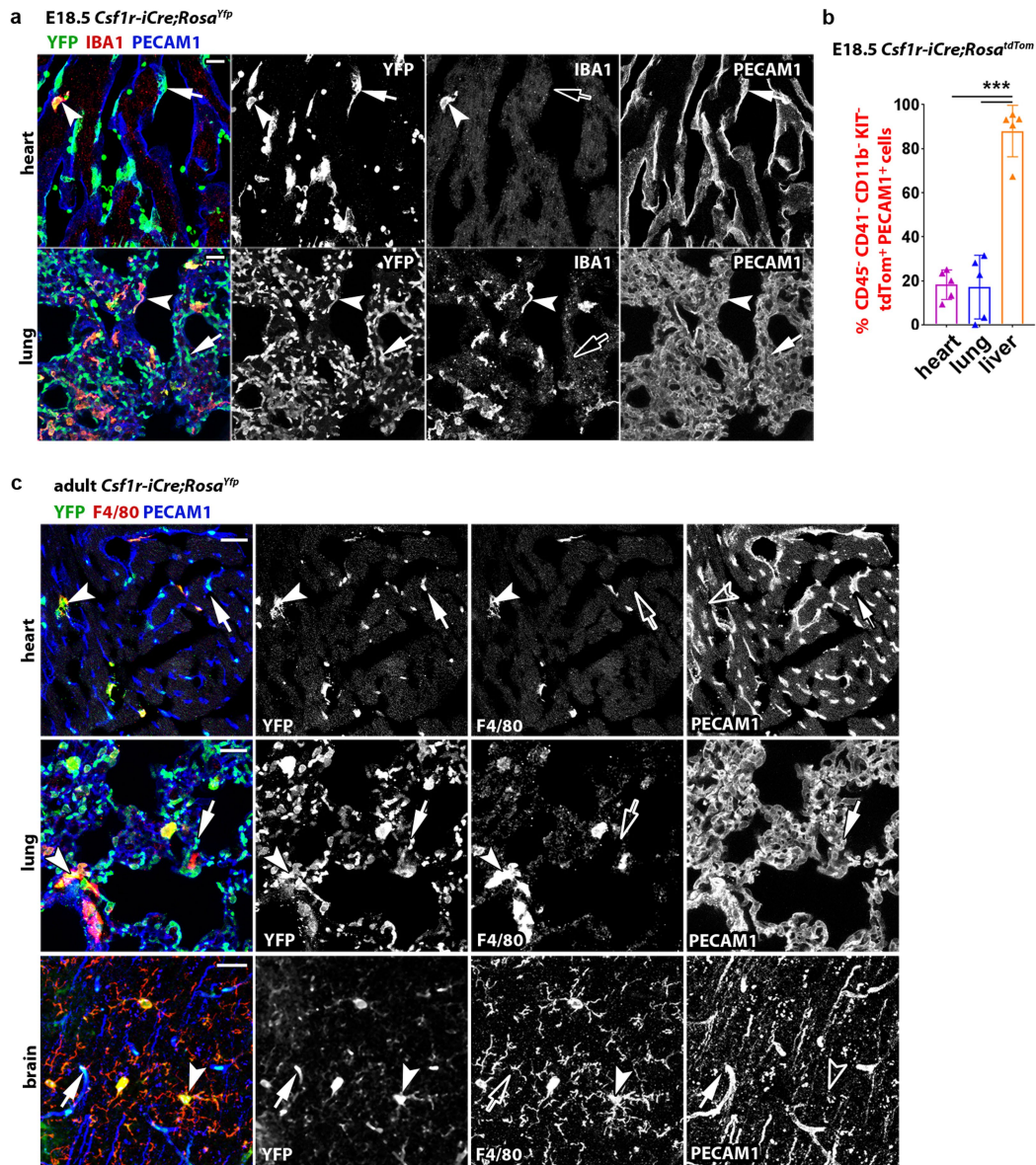


Extended Data Fig. 7 | Validation of gene expression data from RNA-Seq and microarray studies. ECs were FACS-isolated from E12.5 *Csf1r-iCre;Rosa^{tdTom}* embryos ($n = 3$) as in Fig. 6a to validate the RNA-seq and microarray data shown in Fig. 6d–f. *Slc2a1* was analysed as a representative brain EC-enriched transcript/differentiation marker, and *Mrc1* and *Oit3* as representative liver EC-enriched transcripts. **a**, Relative transcript levels of the *Gt(ROSA)26Sor* (*tdTomato*) transcript by RNA-seq of the E12.5 *tdTomato*⁺ and *tdTomato*⁻ EC populations (analysis presented in Fig. 6a–f); mean \pm s.d. of normalized counts, $n = 3$ each; $**P = 0.0085$ (two-sided unpaired *t*-test). **b**, RT-qPCR analysis for the indicated genes in *tdTomato*⁺ versus *tdTomato*⁻ ECs isolated from whole E12.5 embryos ($n = 5$) to validate genes identified by RNA-seq in Fig. 6e, f as differentially expressed. Mean \pm s.d. of fold change; $***P < 0.0001$ (*Slc2a1*), $***P = 0.0008$ (*Mrc1*) $**P = 0.0056$ (*Oit3*) (two-sided unpaired *t*-test). **c**, RT-qPCR analysis for the indicated genes in *tdTomato*⁻ ECs isolated from the E12.5 brain versus liver ($n = 3$ for each organ) to validate organ-specific transcript enrichment identified via microarray analysis shown in Fig. 6f. Mean \pm s.d. of fold change; $*P = 0.019$, $**P = 0.0082$, $***P < 0.0001$ (two-sided unpaired *t*-test); ND, not detectable. **d**, RT-qPCR analysis for the indicated genes to directly compare the expression levels of brain and liver EC differentiation markers in *tdTomato*⁺ versus *tdTomato*⁻ ECs isolated from brain ($n = 3$) or liver ($n = 5$). Mean \pm s.d. of fold change; NS, not significant, $P = 0.9398$ (liver *Slc2a1*), $P = 0.8045$ (liver *Mrc1*), $P = 0.6327$ (liver *Oit3*), $**P = 0.0073$ (brain *Slc2a1*) (two-sided unpaired *t*-test); ND, not detectable.



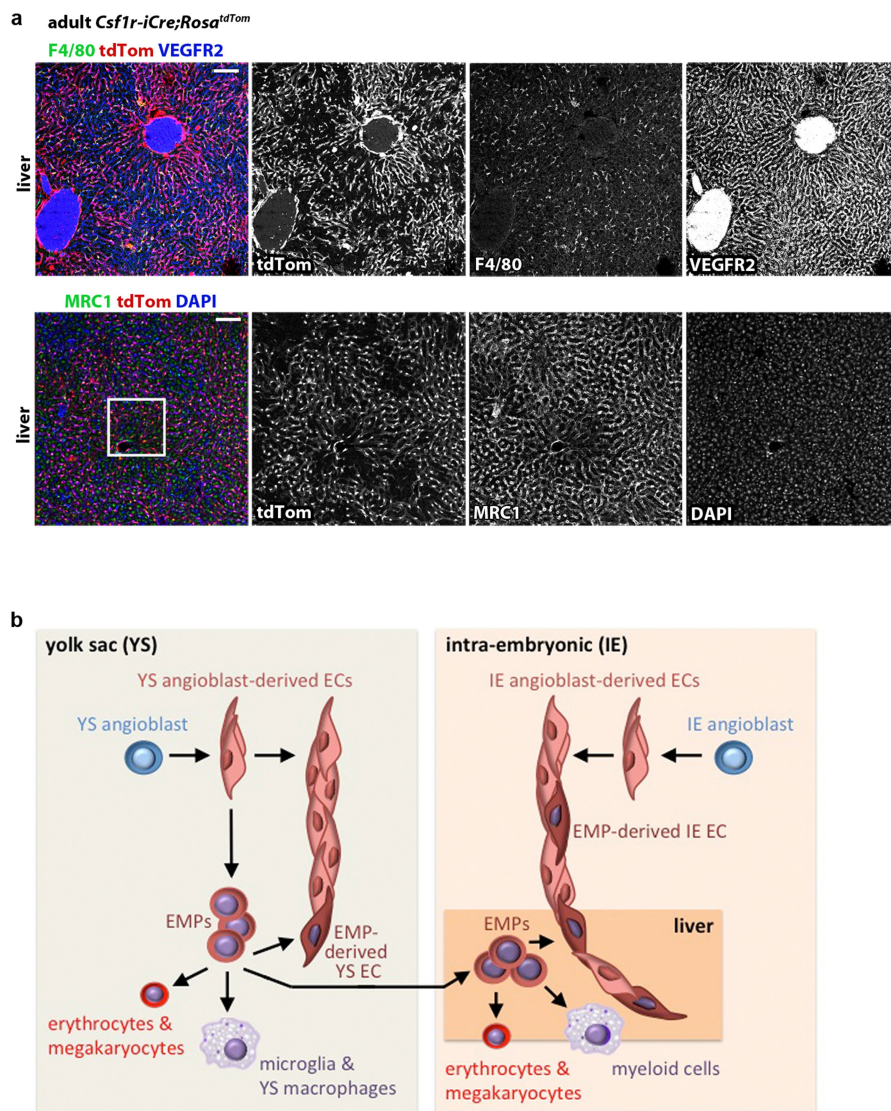
Extended Data Fig. 8 | *Csf1r-iCre*-targeted ECs contribute to embryonic vasculature in multiple organs. **a**, 20- μ m cryosections of the indicated E12.5 *Csf1r-iCre;Rosa^{tdTom}* organs ($n = 3$ each) were immunolabelled for the indicated EC markers together with antibodies for RFP to identify tdTomato protein (top and bottom) or are shown with tdTomato fluorescence (middle); single channels are shown in greyscale. The white boxes indicate the positions of areas shown in higher magnification in Fig. 6g; some areas selected for higher magnification are not contained

entirely within the field of view, and accordingly the boxes are shown incomplete. Scale bars, 200 μ m. **b**, Gating strategy for FACS analysis of tdTomato⁺ and tdTomato⁻ ECs from E12.5 *Csf1r-iCre;Rosa^{tdTom}* brain, lung, heart and liver versus control organs lacking *iCre*, using antibodies for CD11b, CD45, CD41, KIT and PECAM1; associated EC quantifications are shown in Fig. 6i. An analogous strategy was used for the quantifications shown in Fig. 6j and in Extended Data Fig. 9b.



Extended Data Fig. 9 | *Csf1r-iCre*-targeted ECs contribute to organ vasculature in late-stage embryos and adults. **a**, 20- μ m cryosections of the indicated organs from E18.5 *Csf1r-iCre;Rosa^{Yfp}* mice ($n = 2$ each) were immunolabelled for YFP, PECAM1 and IBA1; single channels are shown in greyscale. Arrowheads, YFP⁺IBA1⁺ macrophages; solid and empty arrows, ECs that are YFP⁺ and lack IBA1 expression, respectively. Scale bars, 20 μ m. **b**, FACS analysis of dissociated cells from the indicated organs of E18.5 *Csf1r-iCre;Rosa^{tdTom}* embryos after staining with antibodies for

CD11b, CD41, CD45, KIT and PECAM1, using the gating strategy shown in Extended Data Fig. 8b; mean \pm s.d., $n = 5$ each; *** $P < 0.0001$ (one-way ANOVA, Tukey's multiple comparisons test). **c**, 20- μ m cryosections of the indicated organs from 6-month-old adult *Csf1r-iCre;Rosa^{Yfp}* mice ($n = 3$ organs each) were immunolabelled for YFP, PECAM1 and F4/80; single channels are shown in greyscale. Arrowheads and arrows as in **a**. Scale bars, 20 μ m.



Extended Data Fig. 10 | *Csf1r-iCre*-targeted ECs contribute to adult organ vasculature. **a**, 20- μ m cryosections of 3-month-old adult *Csf1r-iCre;Rosa^{tdTom}* livers ($n = 3$) were immunolabelled for RFP, VEGFR2 and F4/80 or MRC1 and then counterstained with DAPI; single channels are shown in greyscale. The white box indicates an area shown in higher magnification in Fig. 6h. Scale bars, 100 μ m. **b**, Working model for

the role of EMPs in generating extra-embryonic yolk sac and intra-embryonic organ ECs alongside their known role in generating myeloid and erythrocyte/megakaryocyte lineage cells. It is not yet known whether EMP-derived and non-EMP-derived ECs have different functions to regulate normal organ physiology or pathological vascular responses in the adult.

Reporting Summary

Nature Research wishes to improve the reproducibility of the work that we publish. This form provides structure for consistency and transparency in reporting. For further information on Nature Research policies, see [Authors & Referees](#) and the [Editorial Policy Checklist](#).

Statistical parameters

When statistical analyses are reported, confirm that the following items are present in the relevant location (e.g. figure legend, table legend, main text, or Methods section).

n/a Confirmed

- The exact sample size (n) for each experimental group/condition, given as a discrete number and unit of measurement
- An indication of whether measurements were taken from distinct samples or whether the same sample was measured repeatedly
- The statistical test(s) used AND whether they are one- or two-sided
Only common tests should be described solely by name; describe more complex techniques in the Methods section.
- A description of all covariates tested
- A description of any assumptions or corrections, such as tests of normality and adjustment for multiple comparisons
- A full description of the statistics including central tendency (e.g. means) or other basic estimates (e.g. regression coefficient) AND variation (e.g. standard deviation) or associated estimates of uncertainty (e.g. confidence intervals)
- For null hypothesis testing, the test statistic (e.g. F , t , r) with confidence intervals, effect sizes, degrees of freedom and P value noted
Give P values as exact values whenever suitable.
- For Bayesian analysis, information on the choice of priors and Markov chain Monte Carlo settings
- For hierarchical and complex designs, identification of the appropriate level for tests and full reporting of outcomes
- Estimates of effect sizes (e.g. Cohen's d , Pearson's r), indicating how they were calculated
- Clearly defined error bars
State explicitly what error bars represent (e.g. SD, SE, CI)

Our web collection on [statistics for biologists](#) may be useful.

Software and code

Policy information about [availability of computer code](#)

Data collection

listed in methods section

Data analysis

listed in methods section

For manuscripts utilizing custom algorithms or software that are central to the research but not yet described in published literature, software must be made available to editors/reviewers upon request. We strongly encourage code deposition in a community repository (e.g. GitHub). See the Nature Research [guidelines for submitting code & software](#) for further information.

Data

Policy information about [availability of data](#)

All manuscripts must include a [data availability statement](#). This statement should provide the following information, where applicable:

- Accession codes, unique identifiers, or web links for publicly available datasets
- A list of figures that have associated raw data
- A description of any restrictions on data availability

We have provided references to publicly available transcriptomic datasets. We have deposited our own transcriptomic data and provided the accession number.

Field-specific reporting

Please select the best fit for your research. If you are not sure, read the appropriate sections before making your selection.

Life sciences Behavioural & social sciences Ecological, evolutionary & environmental sciences

For a reference copy of the document with all sections, see [nature.com/authors/policies/ReportingSummary-flat.pdf](https://www.nature.com/authors/policies/ReportingSummary-flat.pdf)

Life sciences study design

All studies must disclose on these points even when the disclosure is negative.

Sample size	Sample sizes were not pre-calculated. For histological analyses in Figs. 1, 2, 3 and 4, at least three, but typically more, independent samples (i.e. hindbrains or yolk sacs; for n, see figure legends), were qualitatively analysed by immunostaining, with each experimental repeat yielding highly similar results. Tissue culture experiments were repeated three times with independent samples, with qualitative results obtained by histological examination without associated statistical tests, but results from each experiment being highly similar (Fig. 5). In some experiments (Fig. 6), sample sizes were based on prior published protocols (e.g. Fantin et al., Nature Protocols 2013) and analogous experiments carried out with other strains in our lab (e.g. Fantin et al., Blood 2013). In some experiments (Fig. 2), sample sizes were based on analogous experiments carried out in other genetic background strains in our lab (Fantin et al., Cell Reports 2015). In other experiments, we found that using three independent samples per group gave us sufficient power to detect significant differences between groups, which were then validated by comparing results to published microarray data (i.e. Fig. 7A-E).
Data exclusions	No data exclusions.
Replication	We have reproduced all our results in a minimum of three independent experimental repeats and using independent samples (i.e. by using embryonic materials from several litters). Many experiments were repeated independently by two investigators in the lab, in particular experiments shown in Fig. 1, 2, 3, 4 and 5.
Randomization	Randomisation was not required for our study.
Blinding	Genotype determined group allocation. Data analysis were performed by different staff members responsible for genotyping and analysis, respectively, to avoid conscious and unconscious bias.

Reporting for specific materials, systems and methods

Materials & experimental systems

n/a	Involvement in the study
<input checked="" type="checkbox"/>	<input type="checkbox"/> Unique biological materials
<input type="checkbox"/>	<input checked="" type="checkbox"/> Antibodies
<input checked="" type="checkbox"/>	<input type="checkbox"/> Eukaryotic cell lines
<input checked="" type="checkbox"/>	<input type="checkbox"/> Palaeontology
<input type="checkbox"/>	<input checked="" type="checkbox"/> Animals and other organisms
<input checked="" type="checkbox"/>	<input type="checkbox"/> Human research participants

Methods

n/a	Involvement in the study
<input checked="" type="checkbox"/>	<input type="checkbox"/> ChIP-seq
<input type="checkbox"/>	<input checked="" type="checkbox"/> Flow cytometry
<input checked="" type="checkbox"/>	<input type="checkbox"/> MRI-based neuroimaging

Antibodies

Antibodies used	For all antibodies used, we have provided the catalogue number and supplier. For polyclonal antibodies, which may show batch variation, we have listed the lot number. For monoclonal antibodies, we have listed the clone name.
Validation	All antibodies were sold by the manufacturer with validation data and citations, and they detected the specified targets in our study as expected. Specificity was confirmed by obtaining the expected pattern of tissue staining with the respective antibodies. For example, an antibody to the vascular endothelial protein CDH5 stained only blood vessels, and the F4/80 antibody for macrophages/microglia stained only those cells (e.g. Fig. 1x). YFP and EGFP staining was validated by comparing tissues expressing these proteins or lacking these proteins based on their genetic status (e.g. see Fig. 1A).

Animals and other organisms

Policy information about [studies involving animals](#); [ARRIVE guidelines](#) recommended for reporting animal research

Laboratory animals	We have used laboratory mice for our studies and have reported the strain, genetic background and age for each experiment.
--------------------	--

Laboratory animals	The strains have all been published previously and are described in the methods section with appropriate references. Ages are specified in the figures and figure legends. The vast majority of work was carried out with embryonic material of unknown sex, but, based on Mendelian genetics, all material would be comprised of equal proportions of male and female embryonic tissues, as none of the strains we have used have reported sex-related lethality that would eliminate one or the other sex from litters. Experiments with adult material for Fig. 7 and Extended Data Fig. 5 were also carried out with a mixture of male and female tissues; the sex of the tissues has been recorded and can be provided if required, but is considered not relevant in the context of our study.
Wild animals	The study did not involve wild animals.
Field-collected samples	The study did not involve samples collected from the field.

Flow Cytometry

Plots

Confirm that:

- The axis labels state the marker and fluorochrome used (e.g. CD4-FITC).
- The axis scales are clearly visible. Include numbers along axes only for bottom left plot of group (a 'group' is an analysis of identical markers).
- All plots are contour plots with outliers or pseudocolor plots.
- A numerical value for number of cells or percentage (with statistics) is provided.

Methodology

Sample preparation	listed in the methods
Instrument	listed in the methods
Software	listed in the methods
Cell population abundance	We have specified the relative abundance of all sorted cell populations in each figure panel containing FACS data. Purity was confirmed by qPCR analysis for representative genes in Fig. 2.
Gating strategy	The gating strategy is described in each figure or associated extended data figure. The FSC/SSC gates were determined as described in the methods section. The boundaries between positive and negative populations were determined with FMOs, as described in the methods section.

- Tick this box to confirm that a figure exemplifying the gating strategy is provided in the Supplementary Information.